Ore Geology Reviews 75 (2016) 76–99

Contents lists available at ScienceDirect

Ore Geology Reviews

journal homepage: www.elsevier.com/locate/oregeorev

Nanhuan manganese deposits within restricted basins of the southeastern Yangtze Platform, China: Constraints from geological and geochemical evidence

Chengquan Wu [a,b], Zhengwei Zhang [a,*], Jiafei Xiao [a], Yazhou Fu [a], Shuxun Shao [a], Chaofei Zheng [a,b], Junhua Yao [a,b], Chaoyi Xiao [a,b]

[a] State Key Laboratory of Ore Deposit Geochemistry, Institute of Geochemistry, Chinese Academy of Sciences, Guiyang 550081, China
[b] University of Chinese Academy of Sciences, Beijing 100049, China

ARTICLE INFO

Article history:
Received 2 August 2015
Received in revised form 8 December 2015
Accepted 8 December 2015
Available online 15 December 2015

Keywords:
Nanhuan manganese deposits
Ore genesis
Hydrothermal–sedimentary/diagenetic deposit
Southeastern Yangtze Platform
China

ABSTRACT

The Nanhuan manganese deposits in the southeastern Yangtze Platform occur in the black shale series in the lower part of the Datangpo Formation. In order to constrain the genesis of the deposits, a detailed study was undertaken that involved field observations, major and trace element analyses, organic carbon analyses, and isotope analyses (C, O, S). The major findings are as follows. (1) The ore-bearing rock series, morphology of the ore bodies, and characteristics of ores in several deposits are similar. The ore minerals are rhodochrosite and manganocalcite. The gangue minerals are mainly quartz, feldspar, dolomite, and illite. Minor apatite and bastnaesite occur in the manganese ores. (2) The ores are enriched in Ca and Mg, whereas they are depleted in Si, Al, K, and Ti compared to wall rocks. The ores normalized to average Post-Archean Australian shale (PAAS) are enriched in Co, Mo, and Sr. The chondrite-normalized rare earth element (REE) patterns for ores and wall rocks are between those of typical hydrogenous and hydrothermal type manganese deposits. Additionally, the ores have positive Ce anomalies with an average Ce/Ce* of 1.23 and positive Eu anomalies with an average Eu/Eu* of 1.18 (normalized to PAAS). (3) The average content of organic carbon is 2.21% in the samples, and the average organic carbon isotopic value ($\delta^{13}C_{V\text{-}PDB}$) is −33.44‰. The average inorganic carbon isotopic value ($\delta^{13}C_{V\text{-}PDB}$) of carbonates in Gucheng is −3.07‰, while the values are similar in the other deposits with an average of −8.36‰. The oxygen isotopic compositions ($\delta^{18}O_{V\text{-}PDB}$) are similar in different deposits with an average of −7.72‰. (4) The sulfur isotopic values ($\delta^{34}S_{V\text{-}CDT}$) of pyrite are very high and range from +37.9‰ to +62.6‰ (average of 52.7‰), which suggests that the pyrite was formed in restricted basins where sulfate replenishment was limited. The sulfate concentrations in the restricted basins were extremely low and enriched in $\delta^{34}S$, which resulted in the very high $\delta^{34}S$ values for the pyrite that formed in the manganese deposits. Therefore, a terrigenous weathering origin for manganese can be excluded; otherwise, the sulfate would have been introduced into the basins together with terrigenous manganese, which would have decreased the $\delta^{34}S$ values of pyrites. The manganese, which originated from hydrothermal processes, was enriched in the restricted and anoxic basins, and then, it was oxidized to manganese oxyhydroxide in the overlying oxic waters whereby the products precipitated into the sediments. The manganese oxyhydroxide in the sediment was then reduced to Mn^{2+} and released to the pore waters during the process of diagenesis. Some organic carbon was oxidized to CO_3^{2-}, which made the depletion of ^{13}C in manganese carbonates. Therefore, we suggest that the Nanhuan manganese deposits are hydrothermal–sedimentary/diagenetic type deposits.

© 2015 Elsevier B.V. All rights reserved.

1. Introduction

The Nanhuan manganese deposits, which are located in the southeastern Yangtze Platform, China, occur in the black shale series in the lower part of the Datangpo Formation (Fan and Yang, 1999; Liu et al., 1989). Typical deposits include the Yanglizhang, Dawu, Datangpo, Daotuo, and Xixibao deposits in Guizhou Province, the Xiushan deposit in Chongqing City, the Minle, Xiangtan, and Guzhang deposits in Hunan Province, and the Gucheng deposit in Hubei Province (Fig. 1). The Daotuo (with a reserve of 142 Mt (million tonnes)) and Xixibao (with a reserve of 20 Mt) deposits were discovered during recent explorations, and these new discoveries have increased estimates of manganese resources in the study area to ~400 Mt (Zhou et al., 2013). The average grade of manganese ranges from 15.4% to 22.1% in the study area (Table 1).

* Corresponding author.
E-mail address: zhangzhengw@hotmail.com (Z. Zhang).

http://dx.doi.org/10.1016/j.oregeorev.2015.12.003
0169-1368/© 2015 Elsevier B.V. All rights reserved.

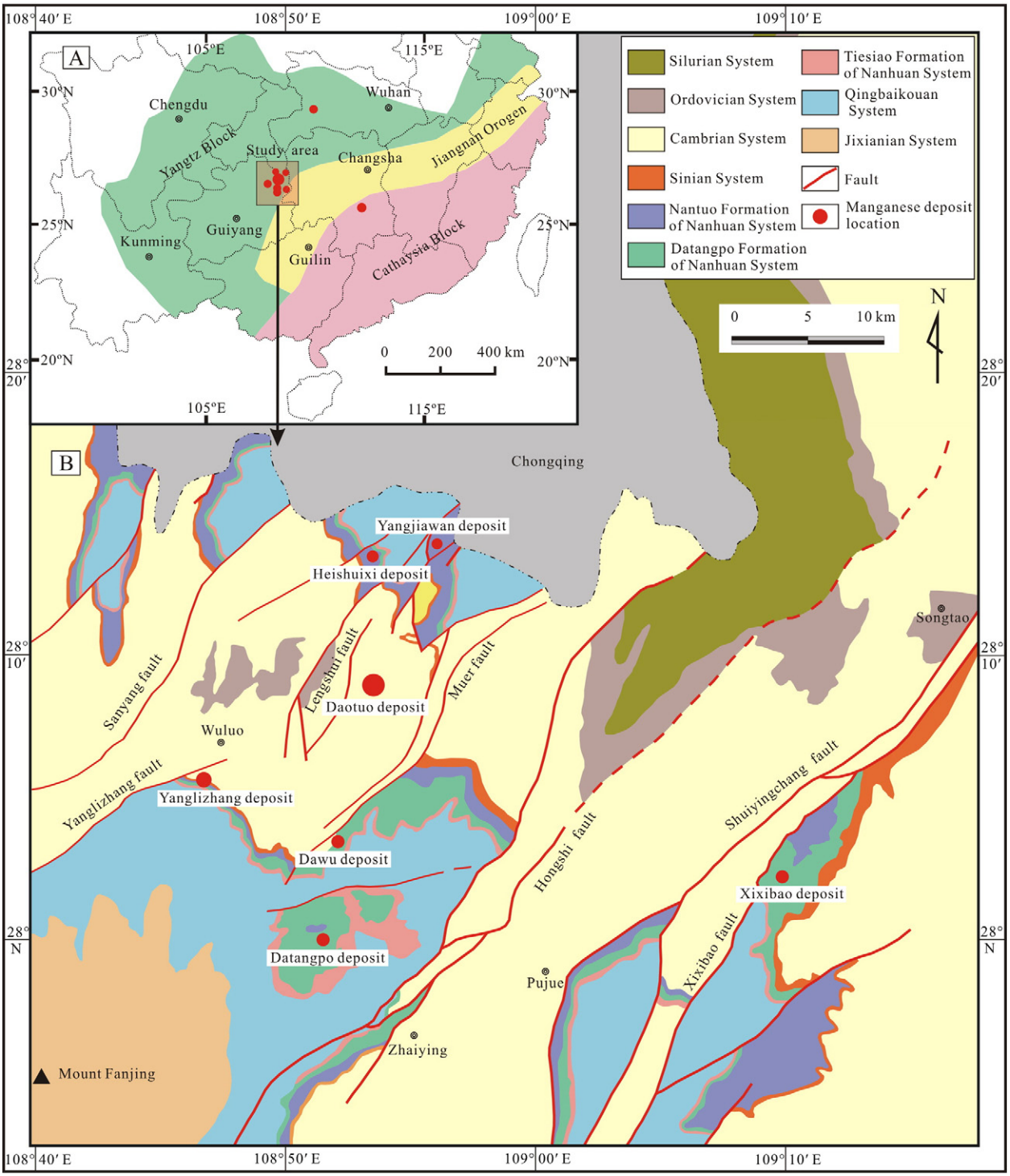

Fig. 1. (A) Tectonic sketch map of South China and the location of the study area. (B) Geological sketch map of the Nanhuan manganese deposits in eastern Guizhou, China. Modified after Zhu et al. (2013).

Many researchers (Chen and Chen, 1992; He et al., 2014; Kuang et al., 2014; Liu et al., 1989; Yang et al., 2002; Yang and Lao, 2006; Zhou et al., 2013) have investigated the mineralization mechanism. However, there are two main unresolved arguments regarding the ore genesis, and views put forth about the ore genesis have been inconsistent. The first one involves the manganese source, and the second one involves the formation of manganese carbonates. There have been controversies about the sources of the manganese in the deposits, and proposed models have included terrigenous weathering (Tang and Liu, 1999), submarine hydrothermal processes (Chen and Chen, 1992; He et al., 2014; Xie et al., 1999), and submarine volcanic activities (Kuang et al., 2014; Yang and Lao, 2006). Regarding the formation of manganese carbonates, some researchers have suggested that they precipitated directly from seawater (Zhou, 2008; Zhou et al., 2013), while others have proposed that they were formed from the reduction of Mn-oxyhydroxides in the sediments (Wang et al., 1985; Zhang, 2014; Zhang et al., 2013a,b). Therefore, different genetic processes for these deposits have been suggested, such as biogenesis (Liu et al., 1989),

Table 1
Characteristics of the Nanhuan manganese deposits in the southeastern Yangtze Platform, China.

Deposit no., latitude, longitude location	Deposit type/ore-hosting stratum	Deposit scale, reserve	Composition and thickness of the ore-bearing rock series	Ore body morphology	Mineral association within the ore body	Ore structure and texture	Grade of metal	Ore-controlling structures
No. 1 Yanglizhang 28°04′13″N, 108°46′42″E Songtao County, Guizhou	Black shale series type/first member of the Datangpo Formation, Nanhuan System	Large 23.4 Mt[a]	The ore-bearing rock series are composed of black carbonaceous shale, manganiferous carbonaceous shale, and rhodochrosite ore bed. Their thicknesses range from 7.5 m to 56.5 m with an average of 27.3 m.[b]	A total of 3 layered ore bodies are bedded and lenticular. Strike NW–SE, dip direction SE, dip angle 35° to 53°, extending to a depth of 1068 m, length 1900 m, thickness 0.71–9.04 m (average of 2.84 m).[c]	Ore minerals: rhodochrosite and manganocalcite. Gangue minerals: mainly quartz and feldspar with minor dolomite, chlorite, pyrite, and apatite.	Micritic, microlitic, and framboidal texture. Massive, banded, and laminated structure.	Mn 14.12–24.79%, average of 19.04%; P 0.142–0.401%, average of 0.234%; TFe 2.58–4.00%, average of 3.30%; belong to high-P, low-Fe, and low-grade type ores.[d]	The deposit is located in the northwestern margin of the Fanjingshan anticline. Ore bodies are controlled by the Yanglizhang fault (Fig. 1B).[e]
No. 2 Dawu 28°02′43″N, 108°51′34″E Songtao County, Guizhou	Black shale series type/first member of the Datangpo Formation, Nanhuan System	Medium 10.3 Mt.[a]	The ore-bearing rock series are composed of black carbonaceous shale, manganiferous carbonaceous shale, tuffaceous sandstone, and rhodochrosite ore bed. Their thicknesses range from 13.0 m to 28.4 m with an average of 18.0 m.[b]	The ore bodies have stratiform-like shapes. Strike NE 65°–70°, length 5500 m, width 500 m, thickness 0.5–3.1 m (average of 1.4 m).[b]	Ore minerals: rhodochrosite and manganocalcite. Gangue minerals: mainly quartz and feldspar with minor dolomite, chlorite, pyrite, and apatite.	Micritic, microlitic, and framboidal texture. Massive, banded, laminated, and cataclastic structure.	Mn 11.10–21.10%, average of 17.11%; P 0.102–0.199%, average of 0.151%; TFe 2.78–6.66%, average of 3.74%; belong to high-P, low-Fe, and low-grade type ores.[b]	The deposit is located in the northwestern margin of the Fanjingshan anticline. Ore bodies are controlled by the Muer fault and Jinzishan anticline (Fig. 1B).
No. 3 Datangpo 27°59′38″N, 108°51′34″E Songtao County, Guizhou	Black shale series type/first member of the Datangpo Formation, Nanhuan System	Medium 9.4 Mt[a]	The ore-bearing rock series are composed of black carbonaceous shale, manganiferous carbonaceous shale, tuffaceous sandstone, dolomite lens, and rhodochrosite ore bed. Their thicknesses range from 10 m to 40 m.[a]	The ore bodies are stratum controlled, and they can be divided into two layers by the boundary with tuffaceous siltstone. Their occurrences are in accordance to the stratum, extending to a depth of 800–1200 m, thickness 0.05–5.74 m (average of 1.68 m).[a]	Ore minerals: rhodochrosite and manganocalcite with minor kutnohorite. Gangue minerals: mainly quartz and feldspar with minor dolomite, chlorite, pyrite, and apatite.	Micritic, microlitic, cryptocrystalline, and framboidal texture. Massive, banded, laminated, and round cavity structure.	Mn 8.87–32.01%, average of 21.63%; P 0.047–0.702%, average of 0.187%; TFe 1.42–12.93%, average of 2.79%; belong to high-P, low-Fe, and low-grade type ores.[a]	The deposit is located in the northwestern margin of the Fanjingshan anticline. Ore bodies are controlled by the NNE, NE, and NNW trending faults.[a]
No. 4 Daotuo 28°07′04″N, 108°52′26″E Songtao County, Guizhou	Black shale series type/first member of the Datangpo Formation, Nanhuan System	Super-large 142 Mt[f]	The ore-bearing rock series are composed of black carbonaceous shale, manganiferous carbonaceous shale, tuff, and rhodochrosite ore bed. Their thicknesses range from 12.5 m to 39.8 m.[g]	A total of 2 layered ore bodies occur as bedded shapes, and they are stratum controlled. Ore bodies in the northern Daotuo syncline strike SE–NW, dip direction SW, dip angle 10° to 18°; in the southern Daotuo syncline strike NE–SW, dip direction NW, dip angle 7° to 26°. Major ore body has a length of 6000 m, width of 4500 m, and thickness of 4–7 m (average of 4.9 m).[g]	Ore minerals: rhodochrosite and manganocalcite. Gangue minerals: mainly quartz and feldspar with minor dolomite, pyrite, and apatite.	Micritic, microlitic, cryptocrystalline, and framboidal texture. Massive, banded, laminated, cataclastic, and round cavity structure.	Mn 10.00–29.21%, average of 18.66%; P 0.139–0.217%, average of 0.173%; TFe 2.32–2.87%, average of 2.69%; belong to high-P, low-Fe, and low-grade type ores.[g]	The deposit is located in the east limb of the Houziao syncline. Ore bodies are controlled by the Muer and Lengshuixi faults (Fig. 1B).
No. 5 Xiushan 28°32′35″N, 108°48′58″E Xiushan County, Chongqing	Black shale series type/first member of the Datangpo Formation, Nanhuan System	Medium 12.9 Mt[h]	The ore-bearing rock series are composed of black carbonaceous shale, manganiferous carbonaceous shale, and rhodochrosite ore bed. Their thicknesses range from 5 m to 26 m.[h]	A total of 3 layered ore bodies have lenticular shapes. Dip direction SE, dip angle 7° to 12°, extending to a depth of 740 m, length 1200 m, thickness 1–3 m.[h]	Ore minerals: rhodochrosite and manganocalcite. Gangue minerals: mainly quartz and feldspar with minor dolomite, pyrite, and apatite.	Micritic, microlitic, and framboidal texture. Massive, banded, laminated, and cataclastic structure.	Mn 13.68–26.55%, average of 22.09%; P 0.099–0.441%, average of 0.215%; TFe 1.57–7.18%, average of 3.14%; belong to high-P, low-Fe, and low-grade type ores.	The deposit is located in the southeast limb of the Tongmaling anticlinorium. Ore bodies are affected by three faults along the margin of the deposit.[h]

No. 6 Minle 28°22′30″N, 109°20′10″E Minle County, Hunan	Black shale series type/first member of the Xiangmeng Formation, Nanhuan System	Large 31.1 Mt[i]	The ore-bearing rock series are composed of black shale, black carbonaceous shale, manganiferous carbonaceous shale, and rhodochrosite ore bed; some dolomite lens can be seen at the top. Their thicknesses range from 0 m to 51.39 m.[i]	A total of 2 layered ore bodies with bedded shapes. Upper ore body: length 1000–5000 m, width 500–1820 m, thickness 0.55–3 m; lower ore body: length 1500 m, width 1290 m, thickness 0.89–1.22 m.[i]	Ore minerals: rhodochrosite and manganocalcite. Gangue minerals: quartz, feldspar, and illite.	Micritic, microlitic, and framboidal texture. Massive, banded, and laminated structure.	Mn 16.01–25.74%, average of 19.79%; P average of 0.253%; TFe average of 2.55%; belong to high-P, low-Fe, and low-grade type ores.[j]	The deposit is located in the center of the Songtao sub-basin of the Wuling fault basin. Regional structures are NE trending, and faults are well developed. The deep fractures containing the Huayuan–Zhangjiajie, Fenghuang–Jishou–Guzhang, and Malichang faults are throughout the region and affect the ore bodies.[j]
No. 7 Guzhang 28°00′21″N, 108°33′34″E Guzhang County, Hunan	Black shale series type/first member of the Xiangmeng Formation, Nanhuan System	Medium 8.8 Mt[i]	The ore-bearing rock series are composed of black shale, black carbonaceous shale, manganiferous carbonaceous shale, and rhodochrosite ore bed. Their thicknesses range from 0.72 m to 19.1 m[k]	A total of 2 layered ore bodies with bedded and lenticular shapes. Upper ore body: length 2800 m, width 1000 m, thickness 0.84–1.60 m; lower ore body: length 800 m, width 200–500 m, thickness 0.52–0.89 m.[i]	Ore minerals: rhodochrosite. Gangue minerals: quartz, feldspar, illite, chlorite, and minor pyrite.	Cryptocrystalline, micritic, microlitic, and framboidal texture. Laminated and massive structure.	Mn 15.58–24.61%; P 0.02–0.24%, average of 0.11%; TFe 1.20–4.60%, average of 3.14%; belong to medium-P, low-Fe, and low-grade type ores.[k]	The deposit is located in the secondary fold of the limbs of the Guzhang anticlinorium.[k]
No. 8 Xiangtan 27°58′52″N, 112°51′25″E Xiangtan City, Xiangtan	Black shale series type/first member of the Xiangmeng Formation, Nanhuan System	Medium 13.1 Mt[l]	The ore-bearing rock series are composed of black carbonaceous shale, manganiferous carbonaceous shale, and rhodochrosite ore bed. Their thicknesses range from 13 m to 32 m.[l]	A total of 3 layered ore bodies occur as bedded and lenticular shapes. The main ore body is within the lower part and has length 1100–2100 m, width 220–1000 m, thickness 0.15–10.46 m (average of 2 m).[l]	Ore minerals: rhodochrosite and manganocalcite. Gangue minerals: mainly quartz, feldspar, illite, and chlorite with minor pyrite, and apatite.	Cryptocrystalline, micritic, microlitic, and framboidal texture. Laminated, banded, and cataclastic structure.	Mn 18.34–23.68%; P 0.120–0.176%; TFe 2.10–2.89%; belong to medium-P, low-Fe, and low-grade type ore.[l]	Ore bodies are controlled by the Xiannv syncline (axial direction NEE–SWW). The fractures are well developed and affect the continuities of ore bodies.[l]
No. 9 Gucheng 30°33′02″N, 111°03′23″E Gucheng County, Hubei	Black shale series type/first member of the Datangpo Formation, Nanhuan System	Medium 12.6 Mt[m]	The ore-bearing rock series are composed of black carbonaceous shale, manganiferous carbonaceous shale, and rhodochrosite ore bed. Their thicknesses range from 12 m to 14 m.[n]	Three layered ore bodies with dip angles 7° to 15°. Main ore body has length 1000–1500 m, width 600–1200 m, thickness 0.48–4.65 m (average of 1.98 m).[m]	Ore minerals: rhodochrosite and manganocalcite. Gangue minerals: mainly quartz and feldspar with minor dolomite, chlorite, pyrite, and apatite.	Micritic, microlitic, and framboidal texture. Massive, banded, laminated, and cataclastic structure.	Mn 15.36–18.99%, average of 17.18%; P 0.202–1.11%, average of 0.77%; TFe 2.44–3.63%, average of 2.85%; belong to high-P, low-Fe, and low-grade type ores.[m]	The deposit is located in the eastern Changyang anticline, which is WE trending and extends 90 km[m]

[a] Guizhou Geological Survey (2009).
[b] Xie et al. (2014).
[c] Hou et al. (2011).
[d] Du et al. (2013).
[e] Regional Geology Department of Geology and Mineral Resources, Ministry of Geology and Mineral Resources (1983).
[f] Ministry of Land and Resources of the People's Republic of China (2014).
[g] Qin et al. (2013).
[h] Cao (2011).
[i] Fu (2005).
[j] Yu (2008).
[k] Ouayang et al. (2011).
[l] Yao et al. (1995).
[m] Tan et al. (2009).
[n] Zhang et al. (2013a).

Yangtze Gorges & central Guizhou	Southern Hubei	Western Hunan	Eastern Guizhou	Northern Guangxi
Doushantuo Fm.	Doushantuo Fm.	Doushantuo Fm.	Doushantuo Fm.	Doushantuo Fm.
Nantuo Fm. (D)	Nantuo Fm. (D)	Nantuo Fm. (D)	Nantuo Fm. (D)	Silikou Fm. (D)
	Datangpo Fm. (Mn)	Xiangmeng Fm. (Mn)	Datangpo Fm. (Mn)	Datangpo Fm. (Mn)
	Gucheng Fm. (D)	Dongshanfeng Fm. (D)	Tiesiao Fm. (D)	Tiesiao Fm. (D)
				Fulu Fm. (Fe)
				Changan Fm. (D)
Liantuo Fm.	Liantuo Fm.	Dieshuihe Fm.	Liangjiehe Fm.	Danzhou Group

Note: |||||| -hiatus; D- diamictite; Mn- rhodochrosite; Fe- iron formation

Fig. 2. Lithostratigraphic units of Nanhuan successions in the southeastern Yangtze Platform, China (Zhou et al., 2004).

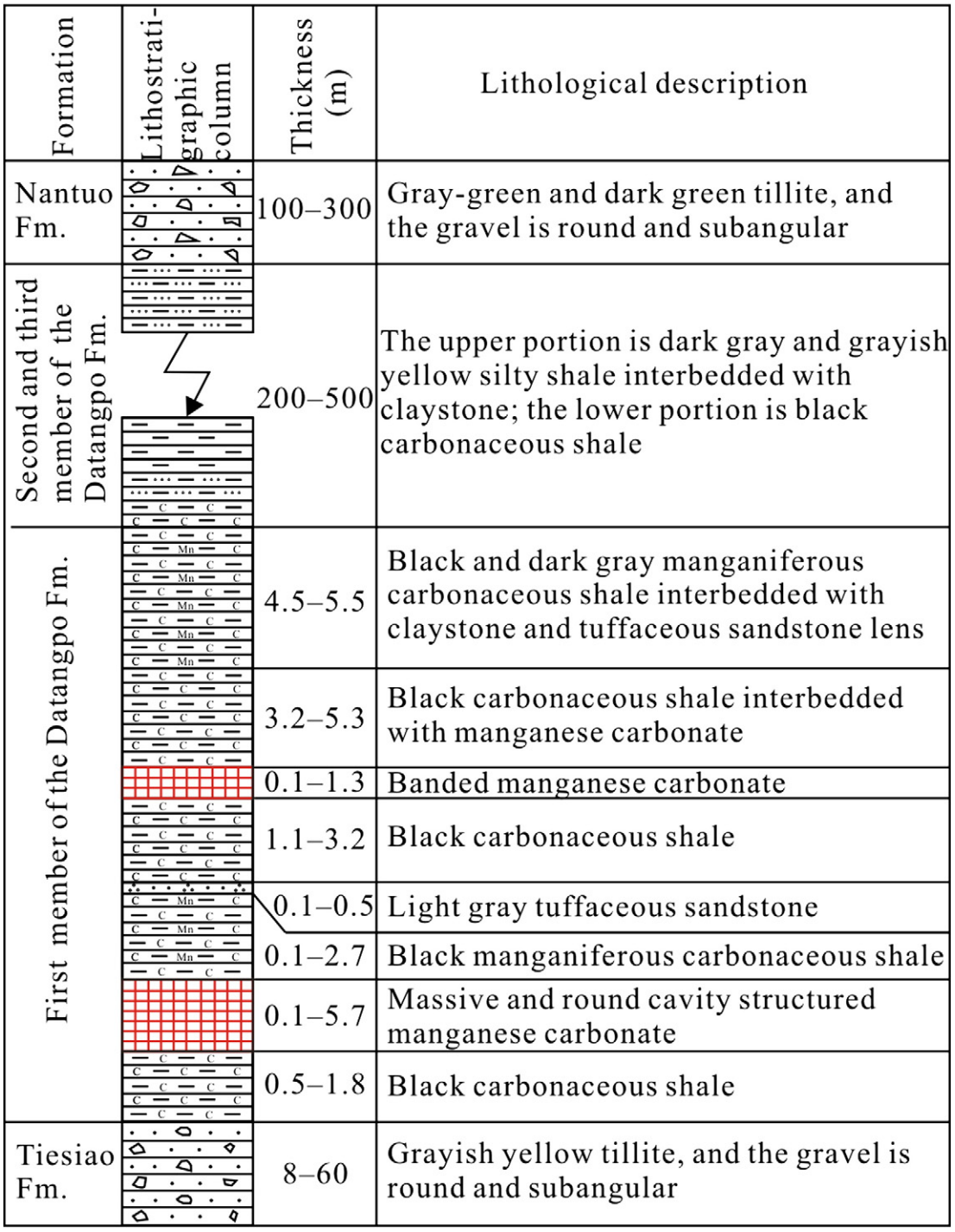

Fig. 3. Stratigraphic details for the Datangpo Formation in the southeastern Yangtze Platform, China (Guizhou Geological Survey, 2009).

hydrothermal sedimentary (Chen and Chen, 1992; He et al., 2014; Wang, 1990), cap carbonate (Yang et al., 2002), submarine volcanic eruption–sedimentary (Kuang et al., 2014; Yang and Lao, 2006), and ancient natural gas seepage (Zhou et al., 2013). While these diverse views give us insight into the mineralization mechanism, they also pose problems for mineral exploration targeting. Hence, in order to constrain the genesis of the manganese deposits, eight deposits including the Yanglizhang, Dawu, Datangpo, Xiushan, Minle, Xiangtan, Guzhang, and Gucheng deposits were selected for our study.

Additionally, paleogeographic reconstruction of the glaciogenic Nantuo Formation suggested that the Nanhuan Datangpo Formation was deposited in the marginal rift Nanhua Basin with only limited connection to the open ocean along its southeastern edge (Li et al., 2012). Previous studies have shown that the ocean of the Nanhuan Period was stratified in the study area with a surface layer consisting of an oxidizing environment and a deep water layer consisting of a reducing environment based on evidence from iron mineral speciation, trace element contents, and sulfur and iron isotopic compositions (Li et al., 2012; Zhang, 2014). The concentration of manganese in solution and its precipitation are primarily redox-controlled (Roy, 2006). Hence, the formation of manganese deposits may be in response to the paleoenvironment change of Neoperoterozoic ocean.

In this study, we provide extensive new data on the ore geology, mineralogy, and element and isotope (C, O, S) geochemistry. Based on our results, we suggest that the Nanhuan manganese deposits were formed in restricted basins and mainly originated from hydrothermal processes. Moreover, the manganese carbonates were formed from the reduction of Mn-oxyhydroxides in the sediments. Therefore, the Nanhuan manganese deposits are hydrothermal–sedimentary/diagenetic type deposits.

2. Geological setting

The study area is located at the conjunction of the Yangtze Block and Jiangnan Orogen (Fig. 1A). The Jiangnan Orogen was formed between ~866 Ma and ~835 Ma (Zhou et al., 2009). At ~866–835 Ma, the oceanic crust, which existed between the Yangtze Block and Cathaysia Block, subducted to the northwest under the Yangtze Block. The collision of the Yangtze Block and Cathaysia Block occurred at ~835–820 Ma, and this event formed the South China Plate (Zhou et al., 2009). The South China Plate broke off at ~820 Ma (Li et al., 2003; Wang and Li, 2003; Wang et al., 2009), and the Nanhua rift was formed. At that time, the southeastern part of the Yangtze Platform was situated on a passive continental margin and a large number of basins were formed along the rift, which provided the advantageous space for deposition of Neoproterozoic lithologies (Jiang et al., 2003; Wang and Li, 2003).

The Neoproterozoic rocks are distributed widely in the study area (Fig. 2), and they take the form of basin facies in eastern Guizhou and western Hunan and transitional and platform facies to the west and north (Zhou et al., 2004). The Datangpo Formation, which hosts the manganese carbonate, is distributed in the basin and transitional facies.

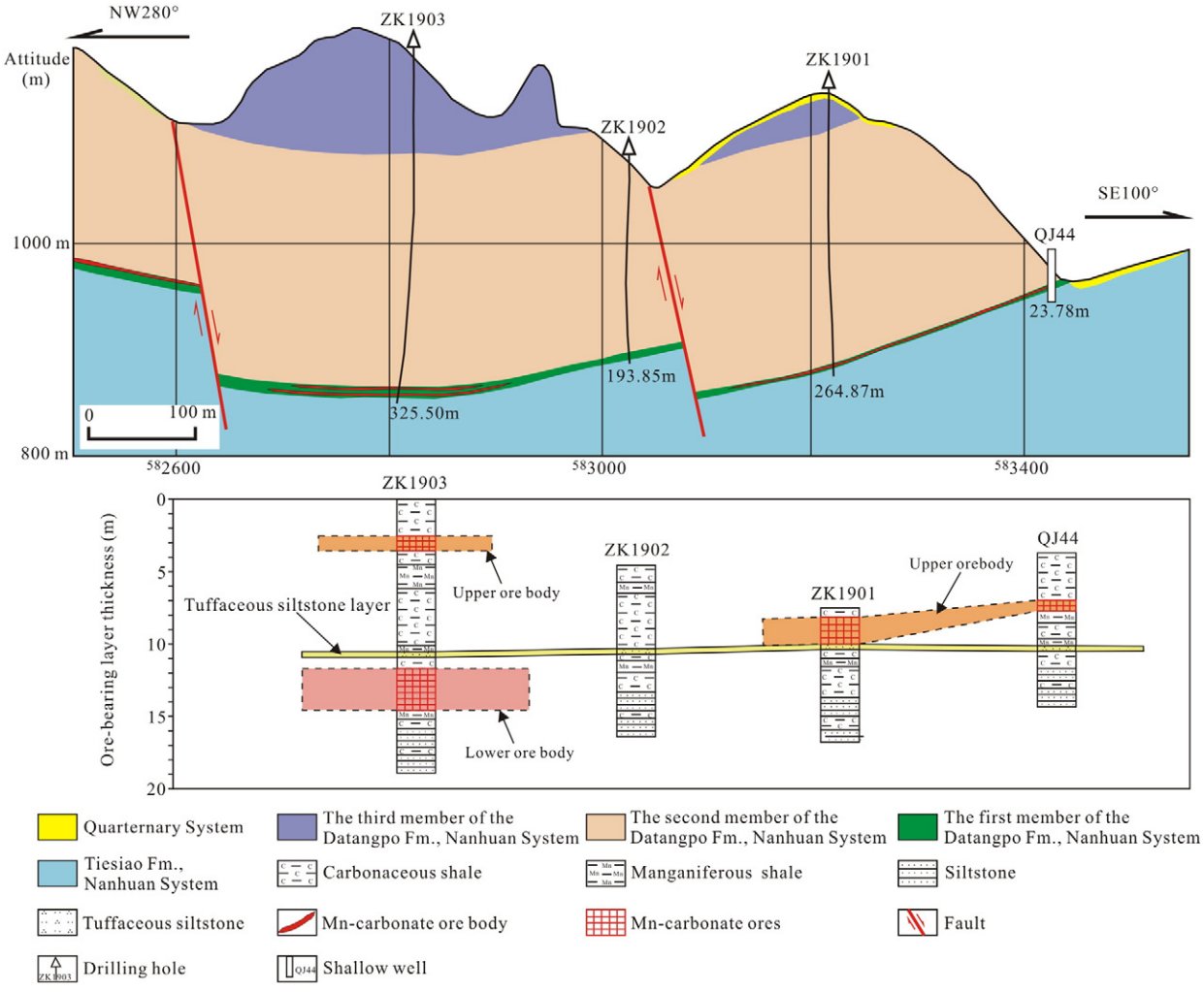

Fig. 4. Geological section along exploration line 19 in the Datangpo deposit (Guizhou Geological Survey, 2009).

The deposition age is constrained from 662.9 ± 4.3 Ma to 654.5 ± 3.8 Ma by the zircon U–Pb ages from interbedded tuff in the lower and upper parts of the Datangpo Formation (Zhang et al., 2008; Zhou et al., 2004). The overlying lithology is the Nantuo Formation, underlain by the Tiesiao Formation; both are in conformable contact (Figs. 2 and 3). The Nantuo Formation is dominated by gray-green and dark green tillite; while the Tiesiao Formation is mainly grayish yellow tillite (Fig. 3). The Tiesiao Formation and Nantuo Formation are both glacial strata that correspond to the Sturtian and Marinoan glaciations in the Cryogenian, respectively (Condon et al., 2005; Macdonald et al., 2010; Zhang et al., 2003b; Zhang et al., 2005; Zhou et al., 2004). The thickness of the Datangpo Formation is 200–500 m. The upper portion is mainly dark gray and grayish yellow silty shale, while the lower portion is mainly black carbonaceous shale (Fig. 3). The manganese carbonates, which are hosted in the black shale series of the first member of the Datangpo Formation, are present in Hunan, Guizhou, Chongqing, and Guangxi, and they are most widely distributed in eastern Guizhou (Fig. 1).

3. Deposit description

The manganese carbonates all occur in the black shale series of the Datangpo Formation, and the ore-bearing rock series, morphology of ore bodies, and characteristics of ores are similar in different deposits. Detailed deposit descriptions are given in Table 1.

The ore-bearing rocks are the black shale series in the lower part of the Datangpo Formation (Figs. 4 and 5A, B), and these are mainly rhodochrosite layers, black carbonaceous shale, manganiferous shale, and interbedded tuff. The thicknesses of ore-bearing rock series range from 14 m to 30 m; these thicknesses have a positive correlation with the thicknesses of ore bodies. They are barren if the thicknesses are less than 10 m (Xie et al., 2014). These rock series can be divided into a

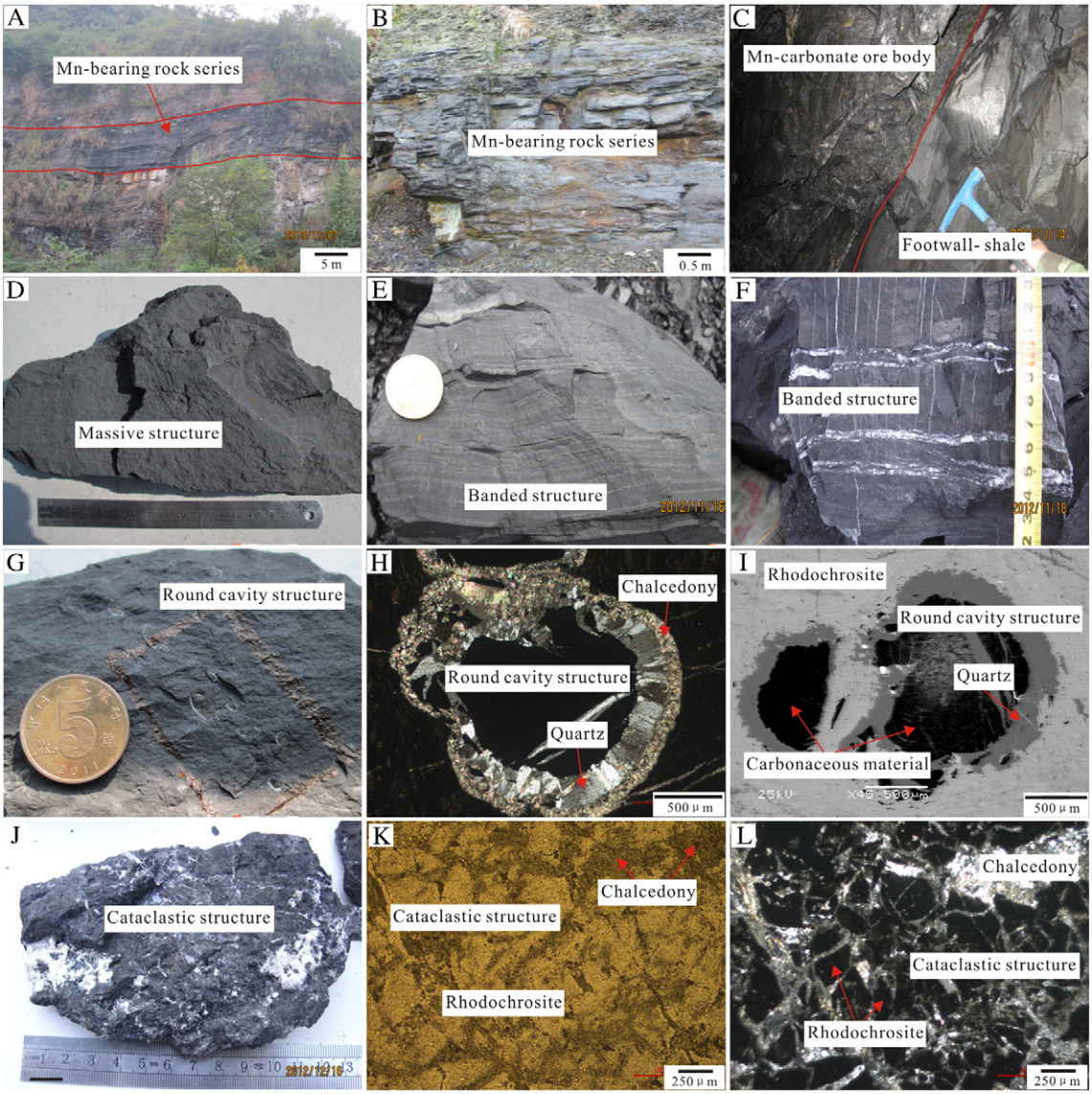

Fig. 5. Manganese-bearing rock series, morphology of ore bodies, and ore structures of the Nanhuan manganese deposits in the southeastern Yangtze Platform, China. (A) Manganese-bearing rock series occur in the first member of the Datangpo Formation; (B) manganese-bearing rock series; (C) manganese carbonate ore body and shale in the footwall; (D) massive structure; (E) banded (laminated) structure, where the laminaes are 0.1–3 mm and mainly composed of rhodochrosite, argillaceous minerals, and carbonaceous material; (F) banded structure; (G) round cavity structure; (H) round cavity structure, where the cavity is composed of quartz and chalcedony zones in the margin (cross-polarized light); (I) round cavity structure, where the cavity is mainly carbonates and carbonaceous material in the core and is surrounded by rhodochrosite (BSE); (J) cataclastic structure, where the fractures of ores are filled by epigenetic quartz, chalcedony, and carbonates; (K) cataclastic structure (reflected light); (L) cataclastic structure (cross-polarized light).

rhodochrosite zone, a carbonaceous shale-manganiferous dolomite zone, and a carbonaceous shale-silty carbonaceous shale zone from the core to the margin of the deposits.

In general, several layered ore bodies occur in the host rock series. The ore bodies occur as bedded and lenticular shapes (Figs. 4 and 5C), and are stratum controlled. The thicknesses of ore bodies vary widely within a range from 0 m to 5 m, and they become thinner from the core to the margin of the deposits. Compared to the upper ore bodies, the lower ore bodies are thicker and of higher grade. The carbonaceous shale, manganiferous shale, and tuff interbeds occur between the ore beds (Figs. 3 and 4). The footwalls are black carbonaceous shales and diamictite, while the hanging walls are black carbonaceous shales (Figs. 3 and 4).

The ore minerals are rhodochrosite and manganocalcite. The gangue minerals are mainly quartz, feldspar, dolomite, and illite. Minor apatite (Fig. 6H) and bastnaesite (Fig. 6K, L) occur in the ores. Rhodochrosite mainly has a micritic and microlitic texture with grain sizes ranging from 2 μm to 6 μm (Fig. 6E, F), and cements are manganocalcite, argillaceous minerals, and carbonaceous material (Fig. 6F). Some rhodochrosites have massive texture and are cemented by argillaceous minerals and carbonaceous material (Fig. 6G). Oolitic textures with rhodochrosite and manganocalcite growing around each other occur in the ores (Fig. 6D). Pyrite is very common in the samples and has a euhedral–subhedral (Fig. 6K, L), framboidal (Fig. 6I), and ring-shaped texture (Fig. 6J). The ores mainly display massive structures (Fig. 5D), banded structures (Figs. 5E, F and 6A, B, C), round cavity structures (Fig. 5G, H, I), and cataclastic structures (Fig. 5J, K, L). The massive ores, which mainly occur in the lower ore bodies, are of a higher grade and composed of rhodochrosite and manganocalcite. The banded ores are most common and occur in two forms. One of these is formed by rhythmic laminaes, which are 0.1–3 mm thick; as such, they also can be called laminated ores. The laminaes are mainly rhodochrosite, argillaceous minerals, and carbonaceous material (Figs. 5E and 6A, B, C). The other form consists of epigenetic quartz veins cutting the manganese carbonate ores

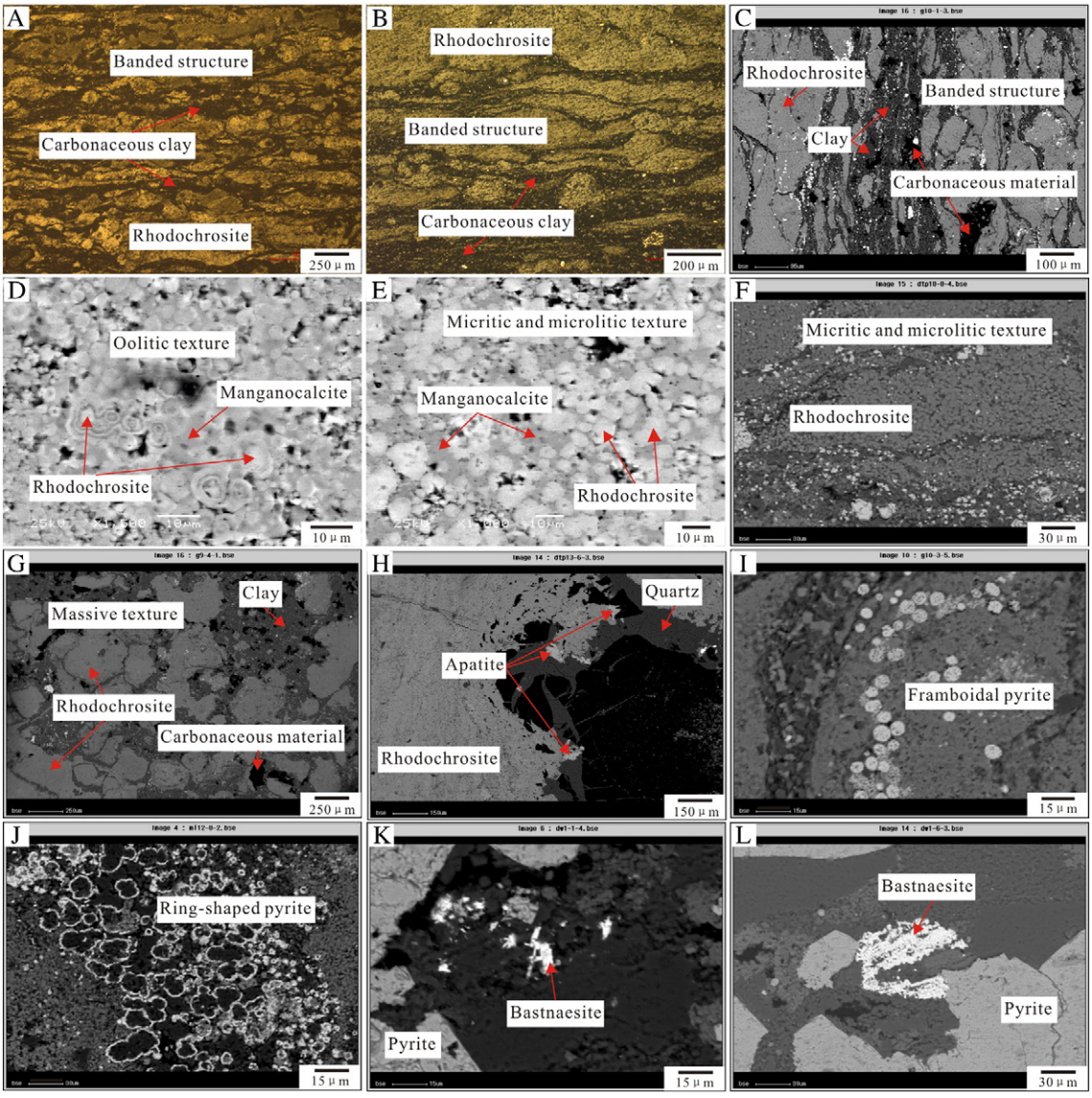

Fig. 6. Ore textures and structures of the Nanhuan manganese deposits in the southeastern Yangtze Platform, China. (A) Banded structure with rhodochrosite and carbonaceous clay (reflected light); (B) banded structure (reflected light); (C) banded structure (BSE); (D) oolitic texture with rhodochrosite and manganocalcite growing around each other (BSE); (E) micritic and microlitic texture, where cements are manganocalcite, argillaceous minerals, and carbonaceous material (BSE); (F) micritic and microlitic texture (BSE); (G) massive texture, where cements are argillaceous minerals and carbonaceous material (BSE); (H) apatite (BSE); (I) framboidal pyrite (BSE); (J) ring-shaped pyrite (BSE); (K) bastnaesite and euhedral–subhedral pyrite (BSE); (L) bastnaesite and euhedral–subhedral pyrite (BSE).

(Fig. 5F). The cataclastic ores were formed when ores were fractured during tectonic activity and were filled by epigenetic quartz, chalcedony, and carbonates. The round cavity structured ores occur only in the Datangpo and Daotuo deposits, and they are of a high grade. The cavities are round or elliptical in shape, and they are 1–12 mm in size. They are composed of quartz and chalcedony zones along the margin, while there are mainly carbonates and carbonaceous material in the core (Fig. 5H, I).

The ores are low-grade, low-Fe, and high-P type manganese carbonates with 12.4–30.0% Mn (average 21.3%), 1.51–7.18% Fe (average 2.76%), and 0.06–1.27% P (average 0.22). The Mn/Fe ratios of ores range from 1.9 to 26.4 (average 8.9), while the P/Mn ratios range from 0.003 to 0.064 (average 0.011).

4. Sampling and geochemical analysis results

4.1. Sampling and analytical methods

Samples were collected from eight deposits including the Yanglizhang, Dawu, and Datangpo deposits in Guizhou Province, the Xiushan deposit in Chongqing City, the Minle, Xiangtan, and Guzhang deposits in Hunan Province, and the Gucheng deposit in Hubei Province. Thirty samples were collected from three profiles in the Dawu and Xiushan deposits (Fig. 7), while others were mainly collected from outcrops, adits, and ore dumps. As shown in Fig. 7, on the profiles, samples were collected perpendicular to the sediment bedding at 5–10 cm internals. The other samples were collected randomly according to rock types, ore structures, and mineral assemblages. These samples included manganese carbonate ores, carbonaceous shales, and manganiferous shales.

All samples were crushed to a 200-mesh size for whole-rock geochemical analyses. The major and trace elements were analyzed at the State Key Laboratory of Ore Deposit Geochemistry, Institute of Geochemistry, Chinese Academy of Sciences. Samples were mixed with $Li_2B_4O_7$ at the following different ratios: (1) 0.7 g of sample (for those samples with Mn < 5%) and 7 g $Li_2B_4O_7$ and (2) 0.4 g of sample (for those samples with Mn ≥ 5%) and 8 g $Li_2B_4O_7$. The samples were then mixed well and melted by a DY501 type electric melting instrument. Then, the major elements were analyzed by X-ray fluorescence (XRF) (instrument was a PANalytical AXIOS, and the method was documented by Hu (2009)). The detection limit for all major oxides was 0.01 wt.%. The analysis errors were less than 3%. Portions (50 mg) of the samples were completely digested using a mixed HF and HNO_3 solution, and then, the trace elements (including rare earth elements, hereafter REEs) were analyzed by inductively coupled plasma-mass spectrometry (ICP-MS) (instrument was an ELAN-DRC-e, and the method was documented by Qi et al. (2000)). The detection limits were as follows: Tb, Ho, Lu, Cs, and Tm, 0.01 ppm; Er, Eu, Sm, Pr, and Yb, 0.03 ppm; Ba, Ce, Co, Th, Gd, Dy, and U, 0.05 ppm; Rb, Cu, Ni, Nb, and Hf, 0.2 ppm; Ta, Nd, Ga, and Sr, 0.1 ppm; Y, Tl, Pb, and La, 0.5 ppm; Zr and Mo, 2 ppm; W and Sn, 1 ppm; V 5 ppm; Cr 10 ppm. The analysis errors were less than 10%.

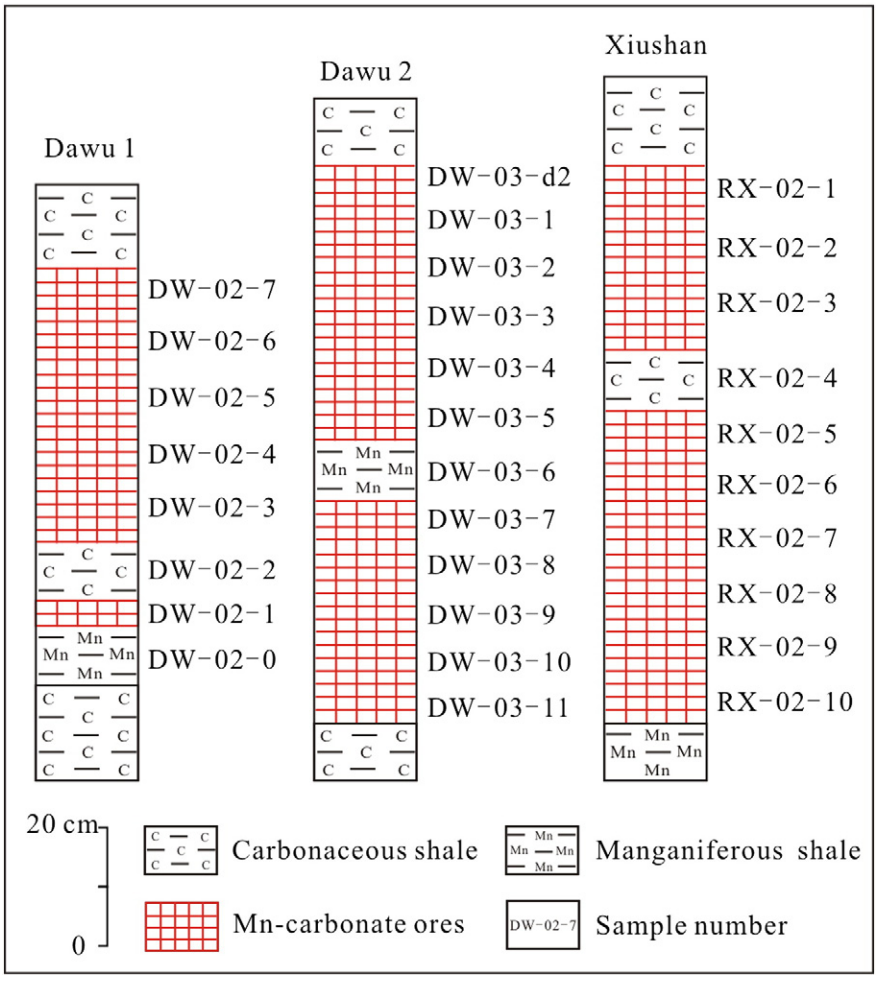

Fig. 7. Schematic diagram of sampling along the profiles in the Dawu and Xiushan deposits.

Table 2
Major element compositions (wt.%) of samples from the Nanhuan manganese deposits in the southeastern Yangtze Platform, China.

Sample	Deposit	Rock (ore) type	Mn	Fe	SiO_2	Al_2O_3	CaO	MgO	K_2O	TiO_2	P	LOI	Mn/Fe	P/Mn
YLZ-03-1	Yanglizhang	Banded ore	25.1	2.64	14.7	1.77	11.0	3.42	0.37	0.10	0.11	31.2	9.50	0.004
YLZ-08-1		Carbonaceous shale	0.74	3.05	65.1	16.1	0.30	0.60	3.76	0.54	0.32	6.76	0.24	0.436
YLZ-08-2		Carbonaceous shale	0.12	3.13	63.3	17.0	0.20	1.06	3.68	0.63	0.05	6.64	0.04	0.436
YLZ-09		Laminated ore	20.3	2.86	22.5	6.66	9.70	2.55	1.89	0.43	0.17	26.3	7.09	0.008
YLZ-01-4		Banded ore	27.2	2.82	8.41	2.61	11.7	2.79	0.80	0.21	0.18	30.8	9.66	0.007
DW-02-0	Dawu	Manganiferous shale	6.17	3.08	55.7	12.2	5.03	2.27	3.09	0.47	0.05	14.3	2.00	0.009
DW-02-1		Laminated ore	15.2	3.24	28.2	6.68	11.6	2.83	1.81	0.36	0.09	25.8	4.70	0.006
DW-02-2		Carbonaceous shale	0.35	2.98	68.0	14.1	0.34	0.61	3.02	0.57	0.15	6.87	0.12	0.436
DW-02-3		Laminated ore	17.1	3.54	26.5	5.18	9.81	3.06	1.46	0.27	0.22	27.3	4.84	0.013
DW-02-4		Laminated ore	16.7	1.75	28.7	6.14	11.3	2.30	1.55	0.29	0.22	26.4	9.54	0.013
DW-02-5		Laminated ore	16.8	2.13	28.9	6.48	10.8	2.63	1.61	0.29	0.17	26.3	7.89	0.010
DW-02-6		Massive ore	25.7	2.58	13.7	1.71	9.07	3.58	0.49	0.09	0.12	33.6	9.98	0.005
DW-02-7		Banded ore	19.6	3.17	27.8	5.98	7.53	2.22	0.34	0.27	0.21	27.8	6.20	0.011
DW-03-d2		Laminated ore	18.6	2.82	31.0	2.64	7.88	2.93	0.45	0.11	0.18	26.8	6.60	0.010
DW-03-1		Massive ore	22.6	4.97	10.4	2.32	11.9	4.84	0.63	0.11	0.11	28.9	4.55	0.005
DW-03-2		Massive ore	23.6	3.65	8.67	1.94	13.5	3.94	0.60	0.13	0.12	29.5	6.45	0.005
DW-03-3		Massive ore	22.2	3.27	13.4	3.41	13.6	3.11	0.95	0.21	0.14	29.8	6.80	0.006
DW-03-4		Laminated ore	17.1	2.44	30.0	6.43	8.79	2.02	0.59	0.27	0.23	26.0	7.02	0.013
DW-03-5		Laminated ore	17.9	2.86	25.0	6.40	11.9	2.96	1.47	0.28	0.19	27.2	6.26	0.010
DW-03-6		Manganiferous shale	3.98	2.17	68.1	11.9	2.70	1.48	2.84	0.44	0.06	10.4	1.84	0.014
DW-03-7		Massive ore	27.2	3.75	12.0	2.18	7.14	3.86	0.43	0.12	0.12	33.2	7.27	0.004
DW-03-8		Laminated ore	24.2	2.65	14.6	1.75	9.08	2.88	–	0.10	0.12	30.8	9.13	0.005
DW-03-9		Laminated ore	25.1	3.39	16.1	2.40	8.32	3.50	0.54	0.12	0.18	31.9	7.42	0.007
DW-03-10		Laminated ore	24.4	3.72	13.9	2.65	8.42	3.66	0.67	0.16	0.22	30.1	6.56	0.009
DW-03-11		Massive ore	23.6	3.19	15.9	2.41	9.54	3.43	0.42	0.13	0.19	29.1	7.40	0.008
DTP-03	Datangpo	Banded ore	24.6	1.50	12.0	1.60	11.7	4.24	0.23	0.10	0.13	32.1	16.37	0.005
DTP-04		Laminated ore	18.8	1.27	13.0	4.14	12.9	5.57	–	0.17	0.11	31.8	14.80	0.006
DTP-11		Laminated ore	15.9	2.41	30.2	5.20	10.3	3.31	1.26	0.31	0.16	26.0	6.60	0.010
DTP-18		Laminated ore	15.2	2.40	27.5	7.92	10.4	3.40	2.01	0.38	0.15	23.6	6.35	0.010
RX-02-1	Xiushan	Laminated ore	18.0	2.46	24.3	7.16	11.5	2.97	2.01	0.33	0.44	25.1	7.31	0.024
RX-02-2		Laminated ore	13.7	7.18	25.7	7.09	9.72	5.72	3.06	0.34	0.27	25.1	1.90	0.020
RX-02-3		Massive ore	22.7	1.57	12.0	3.40	14.8	3.00	0.90	0.16	0.44	31.4	14.41	0.019
RX-02-4		Carbonaceous shale	0.15	3.17	65.5	16.2	0.21	1.05	3.43	0.59	0.06	6.17	0.05	0.436
RX-02-5		Massive ore	24.5	2.18	14.9	3.57	7.49	3.46	0.43	0.19	0.16	31.0	11.22	0.007
RX-02-06		Massive ore	25.8	2.00	13.9	2.50	8.18	3.56	0.47	0.18	0.11	32.2	12.90	0.004
RX-02-7		Massive ore	26.5	2.55	13.2	2.70	8.97	3.25	0.47	0.14	0.10	32.4	10.40	0.004
RX-02-8		Massive ore	19.1	3.93	19.8	4.95	9.46	4.64	1.44	0.23	0.19	28.0	4.87	0.010
RX-02-9		Laminated ore	26.5	2.75	18.6	4.57	8.19	3.75	0.14	0.21	0.24	30.7	9.65	0.009
RX-02-10		Laminated ore	25.7	2.48	14.2	3.87	8.00	4.14	0.78	0.21	0.20	31.4	10.37	0.008
RX-03-1		Massive ore	23.0	3.52	20.4	4.80	7.21	2.82	0.88	0.20	0.12	28.5	6.53	0.005
RX-03-2		Massive ore	22.5	3.60	21.4	4.96	7.56	2.93	0.81	0.31	0.17	28.6	6.25	0.007
RX-03-03		Massive ore	17.0	3.50	32.3	7.56	4.94	2.69	0.59	0.29	0.14	23.8	4.87	0.008
ML-01-1	Minle	Laminated ore	12.4	5.61	33.3	11.7	7.19	7.10	5.75	0.49	0.45	23.9	2.22	0.036
ML-03-3		Laminated ore	21.9	2.37	16.7	5.17	9.65	4.35	1.29	0.30	0.22	29.0	9.28	0.010
ML-03-06		Banded ore	27.6	1.74	15.4	2.41	5.09	3.65	0.27	0.18	0.14	30.9	15.86	0.005
ML-03-10		Massive ore	23.2	1.79	16.6	5.03	8.44	4.05	1.45	0.32	0.20	28.8	12.97	0.009
ML-05		Massive ore	30.3	1.15	9.02	1.75	6.76	4.97	0.39	0.12	0.09	34.4	26.35	0.003
GC-1	Gucheng	Carbonaceous shale	0.65	1.73	61.2	16.7	1.12	1.28	4.92	0.50	0.28	7.55	0.38	0.436
GC-02		Laminated ore	22.4	2.50	19.6	4.53	5.32	3.76	1.34	0.26	0.67	27.8	8.99	0.030
GC-06		Massive ore	22.0	1.96	18.2	5.45	6.05	4.28	1.52	0.19	0.41	28.3	11.19	0.019
GC-07		Massive ore	27.1	1.31	11.1	1.91	6.95	4.25	0.57	0.13	0.63	31.2	20.64	0.023
GC-08		Laminated ore	18.3	2.51	27.8	7.02	3.86	3.62	1.88	0.37	0.39	24.9	7.28	0.021
GC-09		Laminated ore	16.1	3.54	30.7	7.99	3.82	3.92	2.23	0.42	0.46	23.1	4.54	0.029
GC-10		Laminated ore	15.7	3.52	32.1	8.01	2.66	4.28	2.15	0.41	0.15	22.9	4.46	0.009
GC-13		Carbonaceous shale	0.19	5.05	58.6	14.4	0.34	1.88	4.12	0.65	0.08	5.80	0.04	0.436
GC-14		Manganiferous shale	4.16	4.56	50.9	13.6	2.37	4.61	3.82	0.65	0.74	12.7	0.91	0.179
GC-19-1		Massive ore	21.6	1.81	19.3	6.49	5.77	4.11	1.90	0.20	0.30	28.1	11.93	0.014
GC-19-2		Banded ore	19.8	2.39	19.4	4.50	8.56	4.35	1.26	0.22	1.27	26.9	8.29	0.064
GZ-3-1	Guzhang	Carbonaceous shale	0.58	1.85	63.3	16.2	0.54	1.30	4.39	0.58	0.25	8.09	0.31	0.436
GZ-3-2		Carbonaceous shale	0.38	1.75	62.9	16.8	0.39	1.25	4.85	0.47	0.16	7.90	0.22	0.436
GZ-08		Massive ore	14.1	1.91	32.3	9.50	5.42	3.95	2.79	0.24	0.14	23.0	7.37	0.010
GZ-17		Laminated ore	16.8	2.47	26.2	7.07	6.71	4.42	2.25	0.32	0.13	25.9	6.80	0.008
GZ-18		Massive ore	25.3	2.18	13.1	4.08	6.21	5.15	1.28	0.19	0.13	30.3	11.60	0.005
GZ-19		Massive ore	16.4	2.48	26.9	7.02	5.90	4.14	2.23	0.25	0.17	25.5	6.59	0.011
GZ-21		Carbonaceous shale	6.64	3.08	49.2	11.9	2.06	3.64	3.51	0.38	0.05	15.7	2.16	0.007
XT-2-1	Xiangtan	Massive ore	23.3	3.50	10.6	4.07	9.83	5.61	1.18	0.38	0.08	27.1	6.64	0.004
XT-2-2		Massive ore	26.1	2.69	6.63	2.09	11.1	5.17	0.64	0.25	0.08	30.3	9.71	0.003
XT-3		Cataclastic ore	25.4	1.51	16.8	0.51	8.47	4.28	0.19	0.09	0.07	30.1	16.80	0.003
XT-6		Cataclastic ore	21.5	1.49	10.4	1.71	15.8	3.77	0.48	0.12	0.06	31.1	14.44	0.003
XT-7		Laminated ore	15.0	2.98	29.2	7.21	6.56	4.69	2.00	0.41	0.17	23.0	5.04	0.011

LOI = loss on ignition.

The organic carbon analyses, organic carbon isotope analyses, inorganic carbon and oxygen isotope analyses, and sulfur isotope analyses were undertaken at the State Key Laboratory of Environmental Geochemistry, Institute of Geochemistry, Chinese Academy of Sciences. Samples consisted of 1.0 g portions that were sieved through a 200-mesh size screen; after weighing, the samples were

Table 3
Correlations for the major elements in samples from the Nanhuan manganese deposits in the southeastern Yangtze Platform, China.

	Mn	Fe	SiO_2	Al_2O_3	CaO	MgO	K_2O	TiO_2	P
Mn	1								
Fe	−0.21	1							
SiO_2	−0.97	0.13	1						
Al_2O_3	−0.96	0.18	0.95	1					
CaO	0.69	−0.08	−0.79	−0.77	1				
MgO	0.56	0.18	−0.66	−0.54	0.42	1			
K2O	−0.87	0.28	0.82	0.92	−0.66	−0.28	1		
TiO_2	−0.88	0.30	0.86	0.92	−0.68	−0.42	0.86	1	
P	0.00	0.02	−0.03	0.04	−0.06	0.17	0.13	0.07	1

placed into 50 mL centrifuge tubes. In order to remove carbonates, the samples were reacted with 5% hydrochloric acid in a water bath heated to 80–90 °C until the reactions subsided. Then, the residues were washed with deionized water until neutral conditions were reached. The residues were dried at 50 °C, and the organic carbon contents were analyzed by using an organic elemental analysis apparatus (instrument was a vario MACRO cube). The organic carbon isotopes were analyzed with a MAT251EM mass spectrometer. The inorganic carbon and oxygen isotopes were analyzed with a MAT253 mass spectrometer. The carbon isotope and oxygen isotope data are expressed by using international standard V-PDB (Vienna Pee Dee Belemnite) values as follows: $\delta^{13}C_{V\text{-}PDB}$ (‰) = $[(^{13}C/^{12}C)_{sample} / (^{13}C/^{12}C)_{standard} - 1] \times 1000$, $\delta^{18}O_{V\text{-}PDB}$ (‰) = $[(^{18}O/^{16}O)_{sample} / (^{18}O/^{16}O)_{standard} - 1] \times 1000$.

Other samples were crushed to 60- to 80-mesh sizes. Then, light minerals were washed away by using a pan. After that, the pyrite was selected under a microscope. The selected pyrite samples were euhedral–subhedral, as the framboidal pyrites were too small to select under a microscope. A continuous flow-isotope ratio mass spectrometer (CF-IRMS) (EA–IsoPrime instruments) was used (samples were analyzed according to the method documented by Zhou et al. (2014)). The measured data are expressed by using international standard sulfur isotope CDT (Canyon Diablo Troilite) values and sulfur isotope standards GBW04414 (Ag_2S, $\delta^{34}S_{CDT} = -0.07 \pm 0.13$‰) and GBW04415 ($Ag_2S$, $\delta^{34}S_{CDT} = 22.15 \pm 0.14$‰) as follows: $\delta^{34}S$ (‰) = $[(^{34}S/^{32}S)_{sample} / (^{34}S/^{32}S)_{standard} - 1] \times 1000$. The analysis uncertainty was less than ±0.2‰ (2σ).

4.2. Results

4.2.1. Major elements

Major element compositions of samples are shown in Table 2. The ores have 12.4–30.0% Mn (average 21.3%), 1.51–7.18% Fe (average 2.76%), and 0.06–1.27% P (average 0.22). The Mn/Fe ratios range from 1.9 to 26.4 with an average of 8.9, and the P/Mn ratios range from 0.003 to 0.064 with an average of 0.011. The ores are also enriched in Ca and Mg, whereas they are depleted in Si, Al, K, and Ti compared to wall rocks.

The correlation analyses for major elements showed that Mn–CaO (R = 0.69) and Mn–MgO (R = 0.56) have strong positive correlations, while Mn–SiO_2 (R = −0.97), Mn–Al_2O_3 (R = −0.96), Mn–TiO_2 (R = −0.88), and Mn–K_2O (R = −0.87) have strong negative correlations (Table 3 and Fig. 8).

4.2.2. Trace elements

Trace element compositions of samples are shown in Table 4. Compared to average Post-Archean Australian shale (PAAS), the ores are enriched in Co, Mo, and Sr, and they are depleted in V, Cr, Ni, Cu, Zn, Rb, Zr, Ba, Th, and U (Fig. 9A). The PAAS-normalized trace element patterns of wall rocks are similar to those of ores (Fig. 9B).

The ores and wall rocks are similar in REE contents. The REE contents in ores range from 104.01 ppm to 379.95 ppm (average 199.08 ppm), while REE contents in the wall rocks range from 131.63 ppm to 262.06 ppm (average 190.01 ppm).

The PAAS-normalized REE patterns of different deposits are similar (Fig. 10). However, the REE patterns of ores and wall rocks are different (Fig. 11A, B). The ores are enriched in middle rare earth elements (MREEs) (Sm–Ho), and the MREE contents range from 13.38 ppm to 63.87 ppm (average 26.96 ppm). The MREE contents are much lower in wall rocks and range from 8.03 ppm to 32.14 ppm (average 16.96 ppm). The chondrite-normalized REE patterns showed that the patterns of ores and wall rocks are similar and both lie between hydrogenous and hydrothermal deposits (Fig. 11C, D).

The ores have positive Ce anomalies with Ce/Ce* (PAAS-normalized) values ranging from 0.99 to 1.51 (average 1.23), while the wall rocks have no anomalies with Ce/Ce* values ranging from 0.93 to 1.22 (average 1.02) (Table 4). The Eu/Eu* (PAAS-normalized) values in ores are 0.90–1.66 (average 1.18), which represent weakly positive

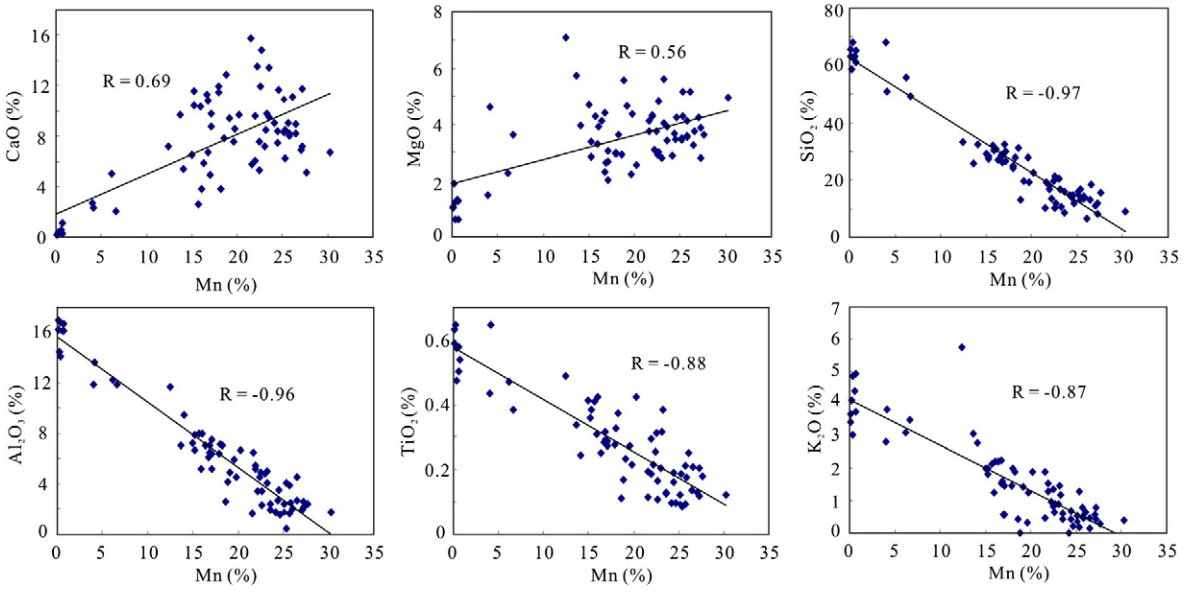

Fig. 8. Correlation diagrams for the major elements in samples from the Nanhuan manganese deposits in the southeastern Yangtze Platform, China.

Table 4
Trace element compositions (ppm) of samples from the Nanhuan manganese deposits in the southeastern Yangtze Platform, China.

Sample	YLZ-03-1	YLZ-08-1	YLZ-08-2	YLZ-09	YLZ-01-4	DW-02-0	DW-02-1	DW-02-2	DW-02-3	DW-02-4	DW-02-5	DW-02-6	DW-02-7	DW-03-d2	DW-03-1	DW-03-2	DW-03-3
Li	7.14	16.6	25.4	6.92	5.31	9.00	9.93	11.2	9.56	11.0	11.3	3.78	109	129	5.63	4.34	6.44
Be	0.43	0.32	0.33	0.00	–	0.16	1.07	0.20	0.43	1.38	1.14	0.30	0.81	1.05	0.35	0.83	0.38
Sc	1.64	14.4	14.0	5.19	2.54	10.9	9.05	12.5	4.94	6.23	6.25	2.03	5.13	2.42	3.26	2.88	3.65
V	22.3	95.6	116	101	50.2	111	85.3	141	57.3	62.5	60.7	22.8	61.2	31.5	38.4	40.5	51.6
Cr	10.3	46.7	43.0	23.3	15.1	51.4	31.7	55.6	24.9	22.2	23.1	10.8	26.9	15.3	29.7	14.3	15.4
Co	41.7	24.0	30.9	50.5	35.7	81.2	52.3	87.1	33.0	23.8	36.4	36.3	54.6	37.2	33.3	28.4	29.0
Ni	11.4	33.6	90.4	20.2	18.8	60.5	42.9	81.3	18.6	12.4	21.9	14.3	28.1	15.0	25.8	16.4	16.9
Cu	6.02	39.2	53.8	16.6	12.9	49.1	38.2	91.5	38.8	8.76	14.2	7.77	23.2	18.1	18.9	12.4	18.1
Zn	17.6	92.1	71.4	36.7	21.1	172	428	101	27.2	59.9	74.2	27.3	31.6	47.9	40.3	23.9	27.2
Ga	9.63	22.9	19.8	15.6	12.0	16.2	16.1	18.1	14.1	14.3	14.9	12.1	13.7	9.89	11.2	11.0	12.7
Ge	0.53	1.88	1.77	0.94	0.40	1.35	1.20	1.73	0.89	0.84	0.80	0.31	1.27	1.65	0.37	0.36	0.48
As	5.17	14.1	18.9	6.80	6.41	11.8	10.4	16.6	7.39	5.58	7.28	6.04	11.0	5.94	7.27	6.50	7.50
Rb	12.3	145	120	60.9	24.0	94.6	54.7	99.6	42.5	48.9	51.9	13.2	26.0	14.3	16.2	16.6	27.9
Sr	409	85.4	60.5	258	386	149	261	88.7	322	285	277	284	592	472	333	364	351
Zr	22.9	182	181	95.5	44.2	154	87.2	201	77.0	89.6	88.2	27.5	95.3	36.8	26.7	32.6	53.6
Nb	5.12	20.3	16.8	17.7	10.7	13.4	9.57	18.1	9.35	9.98	10.2	4.40	11.0	5.36	3.18	4.36	7.09
Mo	1.28	11.3	29.2	0.87	0.95	36.3	9.86	52.4	2.08	4.15	11.7	4.13	7.73	1.42	4.05	2.93	2.51
Ag	–	0.73	0.93	0.47	0.07	0.78	0.48	1.35	0.49	0.29	0.41	–	0.51	–	0.01	–	0.20
Cd	0.05	0.39	0.43	0.09	0.03	1.24	3.52	0.71	0.09	0.37	0.37	0.32	0.15	0.31	0.23	0.12	0.11
In	0.02	0.09	0.11	0.06	0.03	0.10	0.13	0.09	0.06	0.08	0.05	0.06	0.05	0.03	0.06	0.05	0.03
Sn	4.22	4.50	8.31	2.89	3.48	3.95	5.56	7.29	2.80	6.51	3.95	11.6	5.25	6.28	8.60	4.84	5.25
Sb	1.65	10.5	7.83	4.42	3.45	9.26	7.20	12.1	5.13	2.38	3.16	2.15	7.85	2.58	2.92	3.06	4.28
Cs	0.81	7.15	5.37	3.38	1.53	4.52	2.58	5.08	2.43	2.75	2.81	0.94	6.86	2.02	0.86	0.91	1.52
Ba	168	656	630	346	202	461	329	537	285	307	320	184	147	1005	169	161	198
Hf	0.46	5.45	5.03	2.11	0.86	3.91	2.43	5.53	2.04	2.40	2.46	0.71	2.63	0.93	0.78	0.88	1.50
Ta	0.15	1.39	1.07	–	0.24	0.89	0.57	1.29	0.56	0.62	0.62	0.16	0.67	0.23	0.19	0.22	0.46
W	249	35.0	44.9	34.8	83.3	188	51.8	167	78.1	49.7	123	77.0	228	293	82.6	67.1	42.0
Tl	0.09	0.98	0.87	0.39	0.17	0.78	0.42	1.34	0.32	0.27	0.36	0.12	0.32	0.10	0.21	0.17	0.21
Pb	9.57	28.3	66.1	9.20	10.7	31.6	28.8	48.2	26.5	6.37	8.17	6.11	17.5	17.4	14.3	8.88	24.1
Bi	0.04	0.54	0.39	0.13	0.04	0.37	0.19	0.33	0.15	0.18	0.12	0.05	0.13	0.02	0.07	0.08	0.05
Th	1.39	16.3	10.7	5.70	2.57	8.28	5.94	10.8	5.88	6.73	6.59	1.52	6.98	3.21	2.07	2.35	3.89
U	0.50	3.01	2.73	1.35	0.73	2.01	1.77	2.77	1.40	2.02	2.07	0.65	2.34	1.16	0.87	0.98	2.34
Y	22.5	32.7	22.8	31.1	28.8	26.6	40.3	19.2	41.3	46.3	41.4	30.1	39.9	34.3	33.9	39.5	37.6
V/(V + Ni)	0.66	0.74	0.56	0.83	0.73	0.65	0.67	0.63	0.75	0.83	0.73	0.61	0.69	0.68	0.60	0.71	0.75
Th/U	2.78	5.42	3.92	4.22	3.52	4.12	3.36	3.90	4.20	3.33	3.18	2.34	2.98	2.77	2.38	2.40	1.66
V/Cr	2.17	2.05	2.70	4.33	3.32	2.16	2.69	2.54	2.30	2.82	2.63	2.11	2.28	2.06	1.29	2.83	3.35
La	18.4	57.5	32.2	27.0	29.5	36.8	44.6	31.3	39.0	40.6	39.1	24.9	38.5	24.9	26.1	31.6	36.3
Ce	52.4	117	62.5	76.2	80.4	82.4	108	65.8	104	103	99.3	70.0	98.4	68.7	70.5	86.0	94.8
Pr	4.56	12.5	7.04	6.67	6.71	7.46	10.7	6.27	9.88	10.3	9.18	6.03	9.13	6.17	6.64	7.88	8.92
Nd	18.6	44.5	25.7	28.4	26.7	27.7	44.5	21.4	42.0	43.2	36.9	24.5	36.7	25.8	27.4	32.4	36.5
Sm	3.93	7.12	4.64	5.82	5.26	5.29	9.43	3.44	8.36	9.19	7.30	5.12	7.68	5.68	6.32	7.13	7.34
Eu	1.46	1.17	0.79	1.18	1.51	0.96	1.87	0.69	2.39	2.40	1.98	1.26	2.07	1.82	1.43	1.71	1.75
Gd	4.27	5.35	4.15	6.01	5.80	5.01	9.37	3.40	9.10	9.42	8.01	5.53	8.28	6.67	7.33	8.37	7.65
Tb	0.69	0.96	0.67	1.00	0.86	0.78	1.42	0.53	1.29	1.41	1.21	0.91	1.24	1.00	1.20	1.28	1.18
Dy	4.19	6.07	4.08	5.81	5.03	4.45	8.07	3.36	7.61	8.20	7.24	5.43	7.07	6.10	6.98	7.70	6.90
Ho	0.84	1.25	0.90	1.18	1.03	0.89	1.46	0.71	1.54	1.62	1.50	1.07	1.41	1.20	1.28	1.49	1.41
E	2.37	3.76	2.70	3.46	2.99	2.54	4.18	2.45	4.24	4.79	4.32	3.13	4.25	3.42	3.48	4.11	3.97
Tm	0.32	0.56	0.41	0.49	0.41	0.39	0.57	0.39	0.61	0.66	0.63	0.42	0.60	0.46	0.48	0.56	0.57
Yb	1.71	3.68	2.74	2.91	2.38	2.62	3.56	2.61	3.41	3.87	3.55	2.40	3.54	2.60	2.84	3.26	3.30
Lu	0.22	0.56	0.42	0.41	0.30	0.38	0.49	0.38	0.46	0.55	0.48	0.32	0.49	0.37	0.38	0.45	0.44
∑REE	113.97	262.06	148.98	166.49	168.87	177.59	247.96	142.75	234.03	239.40	220.66	150.99	219.34	154.91	162.28	193.86	211.04
Ce/Ce*	1.32	1.01	0.96	1.31	1.32	1.15	1.14	1.08	1.22	1.16	1.21	1.32	1.21	1.28	1.23	1.26	1.21
Eu/Eu*	1.66	0.89	0.85	0.93	1.28	0.88	0.94	0.94	1.28	1.21	1.21	1.10	1.21	1.37	0.98	1.03	1.09

Table 4 (*continued*)

Sample	DW-03-4	DW-03-5	DW-03-6	DW-03-7	DW-03-8	DW-03-9	DW-03-10	DW-03-11	DTP-03	DTP-04	DTP-11	DTP-18	RX-02-1	RX-02-2	RX-02-3	RX-02-4	RX-02-5	RX-02-6
Li	9.72	9.44	4.50	13.0	19.8	12.0	14.8	76.7	14.5	7.01	4.64	4.98	9.08	6.50	5.24	25.2	9.72	8.69
Be	1.25	1.22	–	0.02	0.31	0.47	1.02	1.10	–	–	–	0.34	–	–	–	0.26	–	–
Sc	5.60	6.41	5.76	2.14	1.75	1.83	2.36	2.24	2.24	5.78	5.70	6.51	5.60	5.41	3.27	13.9	3.05	2.20
V	63.7	58.1	86.9	26.3	23.9	29.5	39.4	32.3	47.8	77.7	120	116	68.5	67.8	48.0	98.1	64.7	52.1
Cr	20.7	22.6	35.3	13.9	9.91	13.6	17.7	12.5	11.2	18.2	24.5	29.7	24.9	29.6	15.0	44.9	16.4	11.8
Co	43.7	34.2	120	52.6	34.9	26.8	31.2	26.4	31.1	21.6	35.6	38.0	27.3	61.4	25.0	35.4	35.8	20.6
Ni	27.3	23.8	52.5	21.4	13.3	12.1	14.6	11.4	22.3	26.5	37.4	48.1	14.7	43.7	12.3	80.8	17.5	12.2
Cu	29.9	15.9	45.9	34.9	9.44	17.5	24.5	14.7	20.3	20.1	44.8	47.8	24.9	108	12.0	51.2	12.8	7.58
Zn	33.8	36.8	47.8	42.8	22.9	26.7	42.2	30.0	47.3	42.7	46.2	65.2	56.4	36.1	25.5	84.3	29.5	20.0
Ga	14.7	14.1	14.8	13.0	11.4	11.9	12.5	11.1	9.91	11.5	12.1	15.3	14.4	13.0	10.4	18.8	15.2	14.8
Ge	0.85	0.74	1.17	0.41	0.43	0.56	0.56	0.78	0.54	0.40	0.80	0.80	0.79	0.82	0.39	1.73	0.52	0.47
As	11.6	7.95	15.3	9.12	6.44	5.27	7.87	5.84	5.11	6.02	10.0	6.25	4.84	12.6	4.54	18.4	4.16	3.88
Rb	51.2	46.1	93.9	13.8	11.5	16.3	20.8	13.5	8.10	33.2	41.8	68.2	55.1	62.0	23.3	109	23.0	18.0
Sr	312	367	146	270	321	330	371	476	676	368	300	295	276	241	333	58.7	317	342
Zr	90.9	88.5	159	31.4	31.9	35.9	49.6	36.9	32.2	113	70.7	121	108	105	56.9	187	66.1	44.1
Nb	11.1	10.1	16.5	6.66	6.11	5.71	7.82	6.12	4.00	7.14	10.1	16.3	13.7	14.4	7.32	16.0	9.91	8.57
Mo	3.83	6.35	48.5	3.25	3.09	1.19	1.81	1.08	2.51	9.73	8.64	12.9	0.93	4.75	0.55	23.9	0.61	0.46
Ag	0.47	0.26	1.18	0.03	–	–	0.12	–	–	0.09	0.25	0.80	0.44	1.54	0.02	0.95	0.17	–
Cd	0.17	0.26	0.30	0.08	0.54	0.00	1.62	0.02	0.29	0.34	0.28	0.83	0.46	0.65	0.07	0.43	0.10	–
In	0.04	0.06	0.05	0.04	0.08	0.02	0.18	0.03	0.05	0.05	0.09	0.08	0.09	0.07	0.05	0.11	0.06	0.03
Sn	3.54	4.00	7.45	6.75	21.7	3.70	48.1	3.17	4.75	9.79	2.91	13.0	10.7	9.26	5.08	8.08	7.16	3.37
Sb	7.57	4.66	10.8	4.25	2.72	2.48	3.51	2.69	1.70	1.43	2.81	2.62	1.79	13.3	1.75	7.36	1.62	1.56
Cs	2.71	5.07	5.77	1.50	1.25	1.15	2.28	2.32	1.18	3.28	4.12	5.66	3.86	4.35	1.71	5.12	1.71	1.26
Ba	315	272	461	182	155	162	174	134	151	272	306	460	559	535	357	603	325	313
Hf	2.48	2.42	4.50	0.79	0.79	0.87	1.07	0.93	0.72	1.93	1.99	3.59	2.74	2.50	1.18	5.49	1.26	1.01
Ta	0.65	0.61	1.09	0.19	0.21	0.22	0.51	0.24	0.16	0.37	0.48	0.77	0.60	0.66	0.22	1.03	0.29	0.21
W	36.2	46.6	462	90.2	76.0	85.7	30.0	128	187	36.6	72.2	36.4	62.5	37.2	28.1	95.2	24.8	24.9
Tl	0.36	0.31	1.00	0.18	0.09	0.11	0.15	0.10	0.17	0.39	0.77	0.72	0.29	0.65	0.16	0.84	0.15	0.10
Pb	34.3	14.1	31.5	21.0	7.42	7.31	13.7	7.83	10.0	10.3	23.6	35.4	16.3	88.9	10.5	70.8	11.2	3.43
Bi	0.13	0.13	0.40	0.09	0.02	0.06	0.04	0.08	0.05	0.08	0.17	0.23	0.13	0.16	0.08	0.31	0.09	0.04
Th	7.06	7.07	9.62	1.92	1.86	2.49	3.41	2.83	1.56	4.04	5.80	7.72	5.96	5.37	2.52	10.1	2.95	2.30
U	1.83	2.44	2.45	0.67	0.94	0.76	1.20	0.79	0.50	1.42	1.49	2.08	1.84	1.10	0.71	2.50	0.85	0.62
Y	43.2	45.8	12.8	28.0	25.7	28.2	37.3	33.1	25.1	28.4	26.5	29.0	35.7	28.7	28.9	23.7	22.9	21.3
V/(V + Ni)	0.70	0.71	0.62	0.55	0.64	0.71	0.73	0.74	0.68	0.75	0.76	0.71	0.82	0.61	0.80	0.55	0.79	0.81
Th/U	3.86	2.90	3.93	2.87	1.98	3.28	2.84	3.58	3.12	2.85	3.89	3.71	3.24	4.88	3.55	4.04	3.47	3.71
V/Cr	3.08	2.57	2.46	1.89	2.41	2.17	2.23	2.58	4.27	4.27	4.90	3.91	2.75	2.29	3.20	2.18	3.95	4.42
La	44.9	37.5	30.4	26.6	20.3	22.3	27.5	23.7	19.4	21.8	51.7	36.1	37.0	33.8	26.3	34.6	21.4	19.3
Ce	116	98.0	67.1	74.6	56.2	61.3	77.8	68.0	55.5	59.4	126	87.1	92.0	76.2	71.2	64.5	62.7	55.5
Pr	11.2	9.38	5.21	6.39	4.94	5.49	7.22	6.06	4.93	5.62	10.6	8.24	9.26	6.90	6.48	7.44	5.45	4.85
Nd	45.7	38.6	16.6	25.9	19.8	22.0	29.5	26.2	20.9	22.9	40.2	31.1	36.9	27.6	25.9	27.3	22.6	19.6
Sm	9.11	8.01	2.42	5.39	4.09	4.50	5.94	5.25	4.44	5.03	8.36	5.79	7.74	5.43	5.36	4.77	4.46	4.07
Eu	2.29	1.94	0.57	1.25	1.10	1.46	2.00	1.77	1.33	1.35	2.01	1.56	1.89	1.28	1.54	0.81	1.37	1.27
Gd	9.23	8.68	2.29	5.66	4.48	5.24	6.51	5.83	4.87	5.62	7.75	5.71	7.63	5.01	5.58	4.54	4.40	4.49
Tb	1.40	1.34	0.33	0.88	0.71	0.79	1.04	0.92	0.81	0.92	1.06	0.86	1.15	0.85	0.89	0.74	0.71	0.67
Dy	7.75	8.14	1.94	5.26	4.34	4.77	6.07	5.62	5.01	5.60	5.67	5.05	6.85	4.89	5.35	4.49	4.28	4.18
Ho	1.58	1.67	0.48	1.10	0.94	0.95	1.26	1.20	0.98	1.17	1.08	1.06	1.34	0.97	1.01	0.97	0.82	0.82
E	4.50	4.81	1.72	2.97	2.70	2.92	3.56	3.27	2.84	3.36	2.98	3.17	3.88	2.86	2.97	2.80	2.54	2.41
Tm	0.65	0.69	0.29	0.42	0.35	0.40	0.48	0.47	0.39	0.47	0.42	0.48	0.53	0.41	0.40	0.43	0.36	0.34
Yb	3.86	4.02	2.05	2.27	2.07	2.18	2.97	2.69	2.34	2.76	2.71	3.07	3.14	2.49	2.36	2.84	2.02	1.95
Lu	0.50	0.55	0.30	0.29	0.28	0.30	0.40	0.36	0.33	0.39	0.39	0.41	0.45	0.36	0.33	0.44	0.28	0.26
∑REE	259.19	223.34	131.63	159.03	122.33	134.61	172.26	151.35	124.07	136.43	261.31	189.77	209.79	169.04	155.67	156.64	133.32	119.69
Ce/Ce*	1.20	1.21	1.22	1.32	1.30	1.28	1.27	1.31	1.31	1.23	1.24	1.17	1.15	1.15	1.26	0.93	1.34	1.32
Eu/Eu*	1.17	1.09	1.13	1.06	1.19	1.40	1.50	1.49	1.34	1.19	1.18	1.28	1.15	1.15	1.32	0.81	1.45	1.39

Table 4 (*continued*)

Sample	RX-02-7	RX-02-8	RX-02-9	RX-02-10	RX-03-1	RX-03-2	RX-03-03	ML-01-1	ML-03-3	ML-03-06	ML-03-10	ML-05	GC-1	GC-02	GC-06	GC-07	GC-08
Li	10.5	8.78	9.43	8.49	17.5	19.0	25.0	19.1	67.9	28.2	6.81	7.52	8.29	7.15	4.62	6.79	6.90
Be	–	–	–	–	–	–	–	0.55	0.51	0.09	0.13	–	3.06	1.60	1.39	1.03	1.38
Sc	1.95	5.23	3.07	2.80	3.99	3.70	6.60	10.0	4.67	2.31	3.90	1.71	8.85	3.99	3.66	0.34	6.72
V	53.9	90.9	65.4	59.5	84.3	92.3	117	95.1	93.9	47.1	93.7	35.2	95.0	41.3	110	34.2	49.2
Cr	9.43	21.9	15.7	13.5	19.0	21.1	22.3	37.3	33.3	14.6	30.1	9.58	42.8	32.1	33.9	20.3	38.0
Co	11.2	46.1	38.3	26.9	19.4	32.4	43.2	44.6	46.4	49.8	28.9	31.1	54.2	62.7	53.4	43.7	67.8
Ni	9.04	45.7	20.3	15.6	15.7	21.8	30.7	55.5	29.1	19.8	26.5	13.5	29.9	35.1	38.9	20.8	39.3
Cu	3.68	48.4	16.4	10.6	25.9	61.2	32.6	66.5	26.0	9.32	14.8	8.49	52.5	38.8	37.9	24.4	48.2
Zn	19.9	40.0	27.1	58.6	55.9	48.9	68.1	59.6	35.5	59.5	29.3	43.4	32.9	34.4	35.4	27.1	54.7
Ga	15.2	14.0	14.9	14.7	15.2	15.1	16.0	20.8	15.3	15.4	17.2	13.9	22.5	18.8	18.1	17.5	20.8
Ge	0.48	0.75	0.52	0.50	0.89	0.87	1.08	0.89	0.62	1.20	0.62	0.39	1.26	0.84	0.66	0.49	1.15
As	3.51	8.10	4.66	4.36	2.82	4.30	5.63	34.1	23.6	10.7	9.20	7.54	16.2	6.02	6.11	3.22	7.23
Rb	17.5	38.4	29.2	25.6	30.0	28.1	45.5	94.3	37.4	21.3	43.9	11.9	114	35.8	32.5	16.2	50.3
Sr	351	299	315	319	235	253	213	196	311	234	225	216	98.8	218	186	254	189
Zr	27.7	78.6	67.2	61.0	65.7	76.1	84.2	168	66.8	29.7	75.4	22.7	201	67.3	70.1	41.3	116
Nb	4.62	8.89	8.84	8.29	5.54	8.95	9.47	22.9	14.6	9.92	15.7	7.42	17.3	8.59	4.18	4.08	11.6
Mo	0.77	10.8	0.69	0.65	1.13	1.83	11.0	3.29	5.04	2.57	4.68	1.23	17.6	1.54	3.75	1.18	2.85
Ag	–	0.44	–	0.03	–	0.06	0.19	1.41	0.59	–	0.22	–	0.61	0.24	0.25	0.14	0.38
Cd	–	0.17	0.03	0.25	0.25	0.11	0.54	0.59	0.66	0.14	0.26	0.10	0.15	0.01	0.26	0.04	0.05
In	0.03	0.07	0.04	0.05	0.05	0.06	0.09	0.08	0.10	0.04	0.05	0.03	0.04	0.01	–	–	0.04
Sn	1.77	3.37	5.15	5.64	10.4	6.09	12.8	6.73	19.1	3.35	9.48	3.59	3.66	0.76	0.98	0.28	1.19
Sb	0.82	4.58	2.07	1.54	1.66	3.03	2.83	9.32	4.09	1.18	2.15	0.94	5.72	0.82	3.57	0.60	0.98
Cs	1.12	2.60	2.07	1.86	2.49	2.31	4.08	6.52	4.03	1.36	2.88	0.99	5.89	1.69	1.24	0.74	2.23
Ba	257	415	369	363	319	307	405	528	294	345	439	328	1060	312	507	280	386
Hf	0.71	1.93	1.43	1.36	1.60	1.74	2.22	4.44	1.78	0.86	2.01	0.59	5.13	1.70	1.47	0.89	3.04
Ta	0.17	0.46	0.29	0.28	0.35	0.39	0.52	1.09	0.40	0.21	0.48	0.13	1.07	0.32	0.24	0.15	0.46
W	16.7	39.5	23.6	16.2	23.7	41.1	45.6	27.9	47.6	99.9	20.2	24.4	259	79.5	106	78.2	58.8
Tl	0.07	0.41	0.19	0.15	0.14	0.14	0.31	1.07	0.50	0.19	0.58	0.14	1.02	0.35	0.39	0.22	0.44
Pb	1.91	42.8	10.6	6.19	6.39	16.5	21.9	33.6	17.6	3.62	8.41	10.2	75.6	10.2	9.20	4.53	12.8
Bi	0.04	0.25	0.13	0.06	0.02	0.10	0.14	0.30	0.09	0.04	0.14	0.05	0.37	0.13	0.06	0.08	0.19
Th	1.90	4.49	3.10	3.00	3.37	3.99	5.37	11.2	3.91	1.75	4.49	1.41	12.3	5.96	4.54	3.65	8.39
U	0.48	1.81	1.00	0.65	0.86	1.55	1.27	2.33	1.23	0.72	1.23	0.57	3.37	1.41	1.32	0.99	1.90
Y	19.7	30.1	24.4	23.3	23.7	27.9	24.0	50.8	38.2	30.0	36.9	24.1	38.5	83.6	56.4	74.1	107
V/(V + Ni)	0.86	0.67	0.76	0.79	0.84	0.81	0.79	0.63	0.76	0.70	0.78	0.72	0.76	0.54	0.74	0.62	0.56
Th/U	3.96	2.48	3.10	4.62	3.92	2.57	4.23	4.81	3.18	2.43	3.65	2.47	3.65	4.23	3.44	3.69	4.42
V/Cr	5.72	4.15	4.17	4.41	4.44	4.37	5.25	2.55	2.82	3.23	3.11	3.67	2.22	1.29	3.24	1.68	1.29
La	19.0	26.3	23.6	22.4	20.2	22.4	30.6	48.9	42.2	29.6	41.0	17.9	45.1	40.1	35.7	28.8	53.3
Ce	53.0	70.1	67.1	64.3	53.5	60.8	80.4	118	115	88.3	108	54.9	96.2	104	101	79.9	122
Pr	4.69	6.80	6.00	5.58	5.00	6.12	8.12	12.5	10.3	7.43	9.78	4.66	11.7	12.4	11.0	8.51	15.1
Nd	19.7	28.3	24.5	22.9	21.6	26.7	33.6	50.1	41.4	30.3	37.8	20.6	43.1	53.5	46.1	37.2	63.8
Sm	4.09	6.28	5.05	4.60	4.81	6.32	7.03	10.2	8.99	6.98	7.29	4.63	10.0	11.8	11.2	9.07	15.1
Eu	1.35	1.65	1.54	1.54	1.24	1.65	1.46	1.97	2.03	1.57	1.73	1.05	1.84	2.96	2.45	2.57	3.34
Gd	4.20	6.74	5.22	4.98	5.36	6.78	6.53	10.3	9.10	7.08	7.30	4.90	8.77	12.6	10.8	10.1	15.7
Tb	0.67	1.06	0.79	0.72	0.83	0.99	0.90	1.57	1.28	1.06	1.13	0.78	1.61	2.50	1.98	2.00	3.06
Dy	3.70	5.84	4.51	4.50	4.38	5.71	4.88	9.00	7.58	6.12	6.59	4.75	7.75	14.3	10.8	11.5	18.5
Ho	0.79	1.13	0.89	0.85	0.89	1.06	0.89	1.87	1.47	1.15	1.35	0.93	1.62	3.05	2.23	2.45	4.02
Er	2.07	3.11	2.68	2.44	2.56	3.01	2.74	5.23	4.15	3.29	3.98	2.73	4.28	8.36	5.66	6.67	10.7
Tm	0.30	0.46	0.36	0.36	0.35	0.40	0.37	0.81	0.61	0.44	0.59	0.36	0.62	1.13	0.79	0.83	1.41
Yb	1.72	2.75	2.16	2.09	2.17	2.32	2.21	4.87	3.53	2.58	3.64	2.12	3.62	5.66	4.30	4.50	7.74
Lu	0.24	0.39	0.28	0.27	0.30	0.35	0.33	0.70	0.51	0.34	0.52	0.28	0.58	0.84	0.64	0.64	1.13
∑REE	115.52	160.94	144.63	137.43	123.22	144.55	180.04	275.81	247.62	186.21	230.40	120.59	236.80	273.23	244.68	204.75	334.91
Ce/Ce*	1.30	1.21	1.30	1.33	1.23	1.20	1.18	1.10	1.27	1.37	1.24	1.39	0.96	1.06	1.16	1.17	0.99
Eu/Eu*	1.53	1.18	1.41	1.50	1.13	1.18	1.02	0.90	1.05	1.04	1.11	1.03	0.93	1.13	1.04	1.25	1.02

$Ce/Ce^* = 2(Ce/Ce_N) / (La/La_N + Pr/Pr_N)$; $Eu/Eu^* = 2(Eu/Eu_N) / (Sm/Sm_N + Gd/Gd_N)$, where N indicates that values were normalized to Post-Archean average Australian shale (PAAS) (Taylor and McLennan, 1985); in the table, "–" indicates "below the detection limit."

Table 4 (*continued*)

Sample	GC-09	GC-10	GC-13	GC-14	GC-19-1	GC-19-2	GZ-3-1	GZ-3-2	GZ-08	GZ-17	GZ-18	GZ-19	GZ-21	XT-2-1	XT-2-2	XT-3	XT-6	XT-7
Li	7.89	7.66	11.8	7.32	4.80	4.58	7.63	7.57	5.75	6.06	5.84	5.13	7.94	5.65	4.23	7.51	5.06	14.3
Be	1.83	1.68	1.68	1.86	2.50	1.47	3.28	3.34	3.62	3.33	2.78	3.86	4.15	2.10	1.07	0.65	1.20	3.08
Sc	6.95	7.61	15.4	14.5	4.76	4.79	8.80	6.79	6.51	5.12	1.33	2.45	8.66	1.77	0.21	–	0.30	8.74
V	64.1	68.9	84.3	78.5	123	103	119	88.6	83.9	45.9	30.2	37.7	83.8	102	70.2	43.5	48.8	132
Cr	49.3	52.1	67.8	68.2	40.0	29.3	41.3	33.9	21.5	20.8	13.3	17.2	34.4	26.1	15.6	7.29	10.0	35.5
Co	88.6	87.2	64.0	69.5	56.1	101	62.2	185	84.8	61.2	58.9	65.3	89.9	42.9	37.8	34.0	19.3	52.5
Ni	44.8	44.4	56.8	72.8	37.7	41.4	37.1	28.3	51.7	22.2	22.4	22.9	79.8	47.9	30.6	13.9	17.8	45.3
Cu	52.6	52.4	67.2	89.1	32.7	40.8	47.9	41.6	31.3	18.7	18.7	19.1	28.0	23.3	15.2	8.66	11.1	62.9
Zn	53.0	57.3	70.1	65.8	47.5	38.5	36.4	50.3	125	255	65.8	62.2	91.3	65.9	57.2	30.8	25.3	163
Ga	19.2	19.6	18.6	20.1	19.3	17.3	22.1	23.1	14.9	18.2	17.6	16.9	12.3	19.0	17.4	14.5	13.7	18.1
Ge	1.15	1.11	1.43	1.25	0.82	0.67	1.48	1.47	0.99	0.92	0.48	0.84	1.22	0.41	0.32	0.45	0.34	1.31
As	5.06	4.99	12.6	12.6	5.33	6.07	18.7	16.6	37.3	13.3	27.5	24.9	41.1	84.7	45.3	126	43.8	41.9
Rb	54.7	55.0	99.0	87.4	39.7	32.4	119	121	66.6	56.6	32.2	52.7	85.0	33.0	18.7	6.29	14.6	52.1
Sr	220	216	121	195	211	258	72.1	57.6	171	180	173	161	101	324	320	239	294	324
Zr	101	93.3	160	162	61.8	131	214	201	82.8	113	49.3	84.4	123	120	59.0	22.9	38.1	130
Nb	11.3	11.1	12.4	15.1	4.46	5.55	17.7	14.4	7.77	11.2	8.43	10.5	13.9	29.3	23.9	10.7	6.49	18.0
Mo	1.61	1.89	5.17	2.30	4.37	3.27	12.7	11.0	10.4	3.84	1.43	4.58	31.5	27.0	16.1	6.79	5.90	44.9
Ag	0.29	0.36	0.39	0.46	0.20	0.17	0.78	0.64	0.30	0.40	0.27	0.40	0.52	1.22	0.89	0.26	0.18	0.76
Cd	0.02	0.02	0.04	0.10	0.34	0.33	0.15	0.13	0.38	0.42	0.09	0.09	0.30	0.59	0.21	0.16	0.12	1.42
In	0.03	0.02	0.07	0.09	–	–	0.04	0.04	0.05	0.06	0.01	0.02	0.02	0.01	–	–	–	0.05
Sn	1.27	1.36	2.04	2.19	0.94	0.72	3.41	3.35	1.79	1.44	0.98	1.42	2.00	1.33	0.50	–	0.36	2.24
Sb	0.86	0.78	2.24	1.26	3.08	4.26	6.37	5.23	4.69	3.01	3.95	3.55	7.31	17.9	15.8	3.70	5.63	9.18
Cs	2.74	2.59	4.66	4.91	1.43	1.33	7.56	7.01	2.62	3.11	1.25	2.38	3.81	2.29	1.23	0.33	1.19	4.56
Ba	548	543	802	810	539	462	912	1040	700	533	413	517	699	293	234	229	210	620
Hf	2.68	2.53	4.38	4.47	1.49	1.90	5.53	4.58	2.23	2.70	1.20	1.89	3.03	2.80	1.38	0.50	0.89	3.27
Ta	0.44	0.49	0.76	0.81	0.25	0.24	1.03	0.98	0.36	0.46	0.22	0.31	0.59	0.43	0.22	0.10	0.16	0.60
W	64.3	91.3	107	167	69.1	366	147	556	107	111	46.7	58.2	149	85.9	98.3	143	60.8	109
Tl	0.49	0.55	0.98	1.49	0.38	0.40	0.95	0.85	0.40	0.24	0.22	0.26	0.53	0.56	0.35	0.41	0.98	0.99
Pb	14.1	12.9	181	29.3	8.05	10.0	66.6	64.8	30.9	32.4	31.3	58.5	38.8	104	67.0	17.6	6.31	50.4
Bi	0.23	0.24	0.26	0.29	0.06	0.06	0.33	0.25	0.13	0.12	0.09	0.11	0.21	0.05	0.02	–	0.02	0.15
Th	7.57	7.86	9.93	10.8	4.69	4.28	13.0	10.7	5.87	7.61	3.90	5.89	8.11	4.96	2.44	1.21	3.11	11.5
U	1.95	1.86	2.16	2.50	1.68	1.21	3.63	2.74	2.41	1.59	0.80	1.54	2.65	2.11	1.17	0.45	0.83	3.80
Y	50.8	44.3	23.4	41.9	65.2	80.5	39.6	32.6	64.5	52.2	54.4	56.2	36.5	38.1	33.3	25.5	46.4	99.1
V/(V + Ni)	0.59	0.61	0.60	0.52	0.77	0.71	0.76	0.76	0.62	0.67	0.57	0.62	0.51	0.68	0.70	0.76	0.73	0.74
Th/U	3.88	4.23	4.60	4.32	2.79	3.54	3.58	3.91	2.44	4.79	4.88	3.82	3.06	2.35	2.09	2.69	3.75	3.03
V/Cr	1.30	1.32	1.24	1.15	3.08	3.52	2.88	2.61	3.90	2.21	2.27	2.19	2.44	3.91	4.50	5.97	4.88	3.72
La	39.2	34.9	45.1	46.4	44.5	38.8	40.5	37.8	53.2	46.0	47.1	53.3	42.7	42.4	29.3	14.9	24.7	59.0
Ce	96.1	78.1	90.5	94.6	117	116	87.0	81.4	139	108	120	128	93.3	110	83.4	50.1	75.8	142
Pr	10.4	8.32	10.5	11.3	12.4	13.8	10.1	9.58	15.2	12.0	12.2	14.6	9.75	8.85	6.61	3.93	6.84	17.7
Nd	42.7	31.3	37.2	42.3	55.3	63.1	39.7	36.7	61.5	50.0	49.6	59.5	36.2	32.6	25.8	17.1	28.7	78.1
Sm	9.43	6.84	5.87	9.49	12.6	13.8	6.47	6.51	12.8	10.4	9.39	12.1	4.97	5.74	4.63	3.43	6.21	17.8
Eu	2.24	1.61	0.83	2.00	3.00	3.84	1.18	1.15	2.57	2.41	2.10	2.82	0.99	1.30	1.16	0.83	1.28	3.73
Gd	9.17	6.39	4.28	8.44	12.5	14.3	6.08	5.78	11.8	10.6	9.24	11.6	5.11	6.15	5.46	3.74	6.23	17.4
Tb	1.70	1.32	0.83	1.62	2.25	2.53	1.21	1.04	2.18	1.84	1.77	1.98	1.00	1.10	0.93	0.68	1.24	3.33
Dy	9.58	7.95	4.67	8.79	11.8	13.4	6.77	5.75	11.9	9.77	9.50	10.3	6.09	6.13	5.50	3.81	6.84	17.9
Ho	1.95	1.69	1.02	1.79	2.33	2.77	1.46	1.20	2.41	1.97	1.93	2.06	1.28	1.29	1.11	0.89	1.50	3.71
Er	5.29	4.65	3.10	4.70	6.04	6.96	4.04	3.45	6.35	4.98	5.17	5.64	3.88	3.60	3.21	2.29	4.26	9.75
Tm	0.71	0.68	0.47	0.66	0.80	0.88	0.58	0.48	0.96	0.69	0.72	0.77	0.62	0.58	0.45	0.35	0.62	1.34
Yb	3.82	3.63	2.93	3.83	4.32	4.55	3.62	3.08	5.43	3.89	3.88	4.22	3.99	3.21	2.50	1.71	3.34	7.20
Lu	0.60	0.53	0.42	0.58	0.64	0.65	0.59	0.50	0.82	0.51	0.51	0.62	0.64	0.48	0.35	0.25	0.41	0.99
∑REE	232.89	187.91	207.72	236.50	285.43	295.40	209.31	194.42	326.10	263.01	273.11	307.49	210.51	223.43	170.41	104.01	167.97	379.95
Ce/Ce*	1.10	1.06	0.96	0.95	1.14	1.13	0.99	0.99	1.12	1.06	1.15	1.05	1.06	1.31	1.38	1.51	1.34	1.01
Eu/Eu*	1.13	1.15	0.77	1.05	1.12	1.28	0.89	0.88	0.98	1.08	1.06	1.12	0.92	1.02	1.07	1.08	0.96	1.00

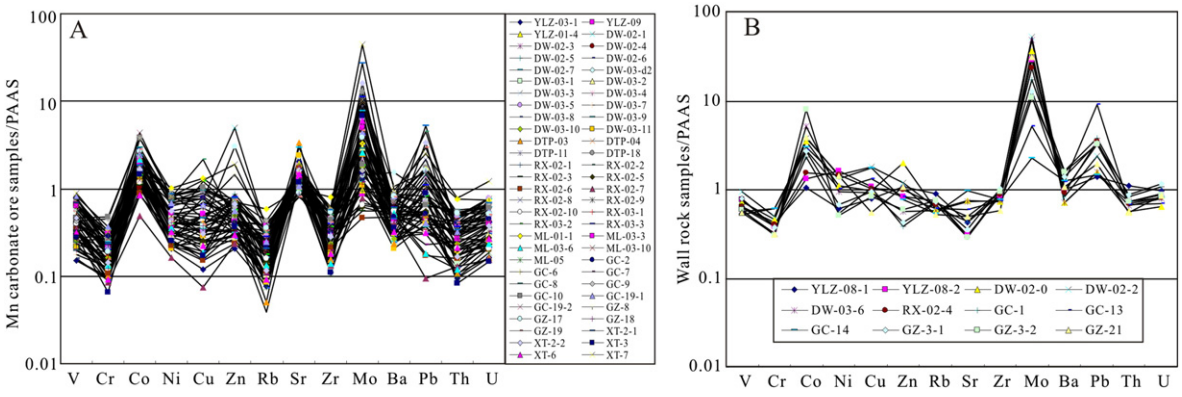

Fig. 9. PAAS-normalized trace element patterns of (A) ores and (B) wall rocks from the Nanhuan manganese deposits in the southeastern Yangtze Platform, China. The PAAS data are from Taylor and McLennan (1985), and the "sample no." is the same as that in Table 2. NASC: North American shale composite.

anomalies, while wall rocks have weakly negative anomalies with Eu/Eu* values ranging from 0.77 to 1.13 (average 0.91) (Table 4).

4.2.3. Contents of organic carbon, organic and inorganic carbon isotopic compositions, and oxygen isotopic compositions

Organic carbon contents, organic and inorganic carbon isotopic compositions, and oxygen isotopic compositions of samples are shown in Table 5. Twenty-two samples from two profiles in the Dawu and Xiushan deposits were selected for carbon content and organic carbon isotope analyses. The results showed that the organic carbon contents and organic carbon isotopic compositions ($\delta^{13}C_{V\text{-}PDB}$) have no obvious changes along the profiles. The total organic carbon contents (TOC) range from 1.37% to 3.43% with an average of 2.21%, and the organic carbon isotopic compositions range from −32.07‰ to −33.97‰ with an average of −33.44‰.

The inorganic carbon isotopic compositions ($\delta^{13}C_{V\text{-}PDB}$) of carbonates in Gucheng, which range from −2.41‰ to −4.02‰ (average −3.07‰), are different from those in the other deposits, which range from −6.33‰ to −10.84‰ (average −8.36‰). The oxygen isotopic compositions ($\delta^{18}O_{V\text{-}PDB}$) are similar in different deposits, which range from −3.59‰ to −12.71‰ with an average of −7.72‰.

4.2.4. Sulfur isotopic compositions of pyrite

The results for sulfur isotopic compositions of pyrite are shown in Table 6. The $\delta^{34}S$ values of pyrite have the following characteristics. (1) They are very high and range from +37.9‰ to +62.6‰ with an average of +52.7‰ (Table 6, Figs. 12 and 13A); the values are similar in manganese ores and wall rocks. (2) The histograms from 205 samples show that the $\delta^{34}S$ have values ranging from +46‰ to +59‰ (Fig. 13B). (3) The $\delta^{34}S$ values decrease from the bottom up along the profiles. The $\delta^{34}S$ values decrease from +63.0‰ to +56.2% in the samples along the drill hole in Daotuo (Zhu et al., 2013); they also decrease from +52.3‰ to 49.0‰ in the Yanglizhang profile (Liu et al., 1989) and from +49.3‰ to +37.9‰ and +49.3‰ to 36.9‰ and in the Dawu 1 and 2 profile, respectively (Fig. 14). (4) The $\delta^{34}S$ values differ significantly for different deposits. Based on our data, we found the following order: Dangtangpo (average 61.8‰) > Minle (average 58.1‰) > Yanglizhang (average 52.2‰) > Dawu (average 47.3‰), which is similar to the order in the literature (i.e., Dangtangpo (average 54.0‰) > Minle (average 52.7‰) > Yanglizhang (average 48.8‰) > Dawu (average 44.5‰)) (Table 7) (Feng et al., 2010; Li et al., 1996; Li et al., 1999; Li et al., 2012; Tang, 1990; Tang and Liu, 1999; Wang et al., 1985; Zhou, 2008). (5) The variations of $\delta^{34}S$ values are within a narrow range, for instance, they range from 61.3‰ to 62.6‰ in 6 samples from Datangpo, from 43.7‰ to 50.9‰ in 9 samples from Dawu, and from 56.2‰ to 63.3‰ in 10 samples from Daotuo (Zhu et al., 2013) (Tables 6 and 7). (6) The average $\delta^{34}S$ values have a strong negative correlation with the average Fe contents, and the correlation coefficient (R) is −0.83 (Fig. 15).

5. Discussion

5.1. Origin of the manganese deposits

There have been controversies about the sources of the manganese in the deposits, and proposed sources have included terrigenous weathering (Tang and Liu, 1999), submarine hydrothermal processes (Chen and Chen, 1992; He et al., 2014; Xie et al., 1999), and submarine volcanic activities (Kuang et al., 2014; Yang and Lao, 2006). Tang and Liu (1999) studied the mineralogy and microfossils of Minle deposit and suggested that the deposit mainly originated from weathering of continental rocks and that volcanic eruptions on the seafloor and fluids from the deep mantle contributed some amount of Mn to the deposit. They proposed that the carbon of manganese carbonates was derived from the oxidation of oceanic organic matter and seawater bicarbonate, as the ores had negative $\delta^{13}C_{PDB}$ values (−8.6‰ to −11.3‰) (Tang and Liu, 1999). Kuang et al. (2014) and Yang and Lao (2006) found that volcanic debris was common in manganese-bearing series from the Nanhuan manganese deposits in northwestern Hunan. Moreover, the manganese grades had positive correlations with the amounts of volcanic debris (Kuang et al., 2014). Therefore, they suggested that the manganese deposits mainly originated from submarine volcanism (Kuang et al., 2014; Yang and Lao, 2006). Zhou et al. (2013) found that the Nanhuan manganese deposits were strictly controlled by the ancient faults. Additionally, the diapir, pipe and mud-type volcanic structures were found to be common occurrences in the manganese-bearing rock series (Zhou et al., 2013). These data were interpreted to mean that the manganese deposits had formed as the result of ancient natural gas seepage (Zhou, 2008; Zhou et al., 2013). They suggested that the carbon in the manganese carbonates was derived from inorganic methane, which had formed from mantle degassing, as the manganese carbonates and inorganic methane have similar carbon isotopic compositions (Zhou, 2008; Zhou et al., 2013). Chen and Chen (1992) and He et al. (2014) proposed a model in which it was suggested that Mn mainly originated from hydrothermal processes. The evidence for this hydrothermal sedimentary model was as follows: (1) the element geochemistry of manganese-bearing rock series, such as the ratios of Al/(Al + Fe + Mn), (Fe + Mn)/Ti, and Co/Zn, and the samples in the diagrams of (Cu + Ni + Co) × 10-Fe–Mn and Co/Zn–(Cu + Ni + Co) are similar to those of hydrothermal sediments; and (2) the homogenization temperature of quartz inclusions in the ores is 194 °C, while the temperatures deduced by the bitumen reflectance (2.5% to 4.0%) are 170 °C to 195 °C.

The manganese deposits are located in the southeastern Yangtze Platform. Neoproterozoic rifted margins are present in the study area

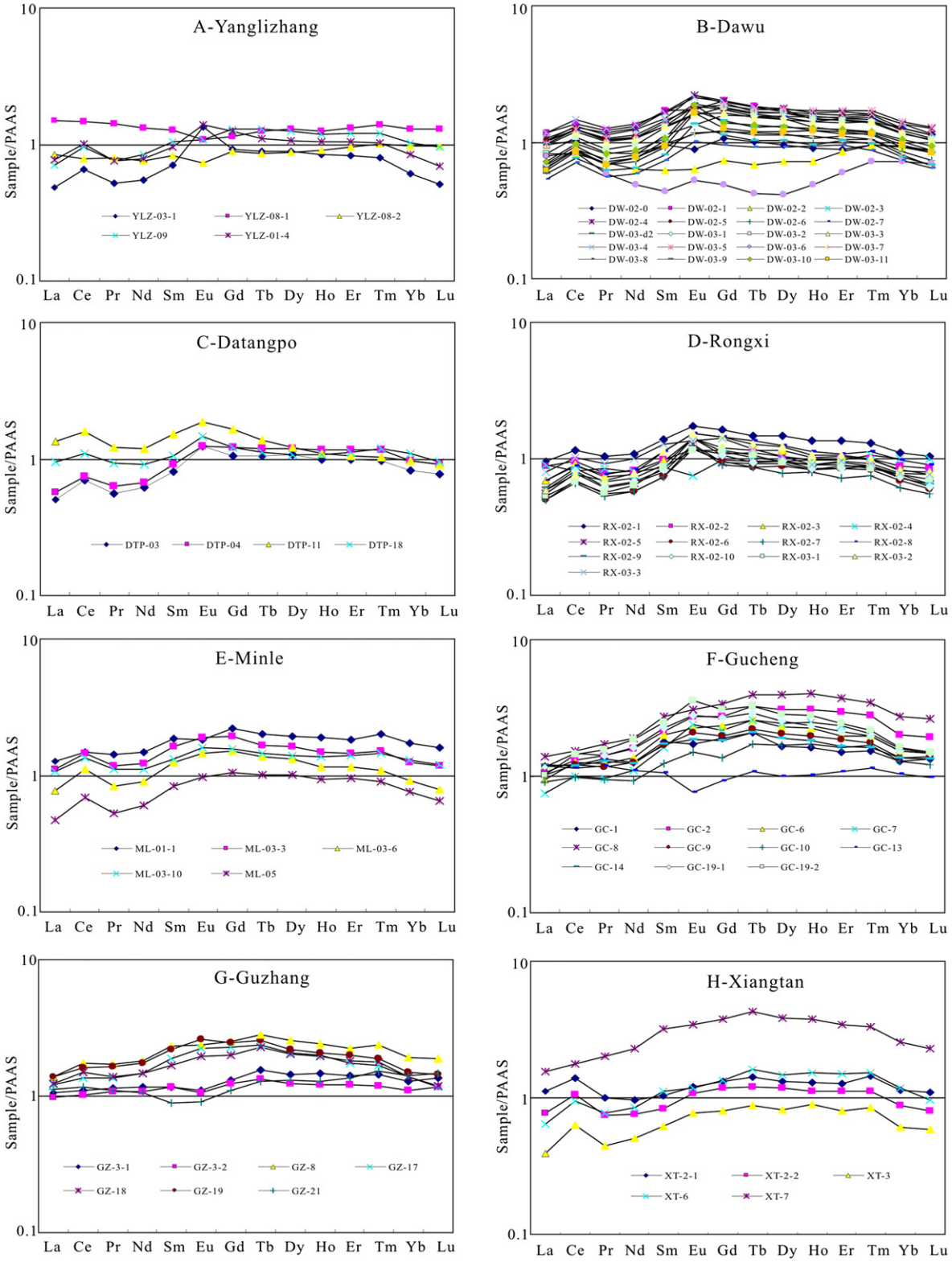

Fig. 10. PAAS-normalized REE patterns of samples from the Nanhuan manganese deposits in the southeastern Yangtze Platform, China. The PAAS data are from (Taylor and McLennan, 1985), and the "sample no." is the same as that in Table 2.

along with a large number of rift basins, which provided the necessary space for deposition of Neoproterozoic sediments (Jiang et al., 2003; Wang and Li, 2003). The distributions of manganese deposits and fault depression basins are controlled by NE trending paleo-faults (Figs. 1 and 12). These faults also could have provided the channels for manganese. In addition, terrigenous weathering was probably a manganese source as the study area was situated on the continental margin.

The ore-bearing series rocks generally contain tuffaceous siltstone layers. However, tuffaceous siltstone layers only exist in the lower portion of ore-bearing series rocks and their thicknesses range from a few centimeters to tens of centimeters. Therefore, submarine volcanic

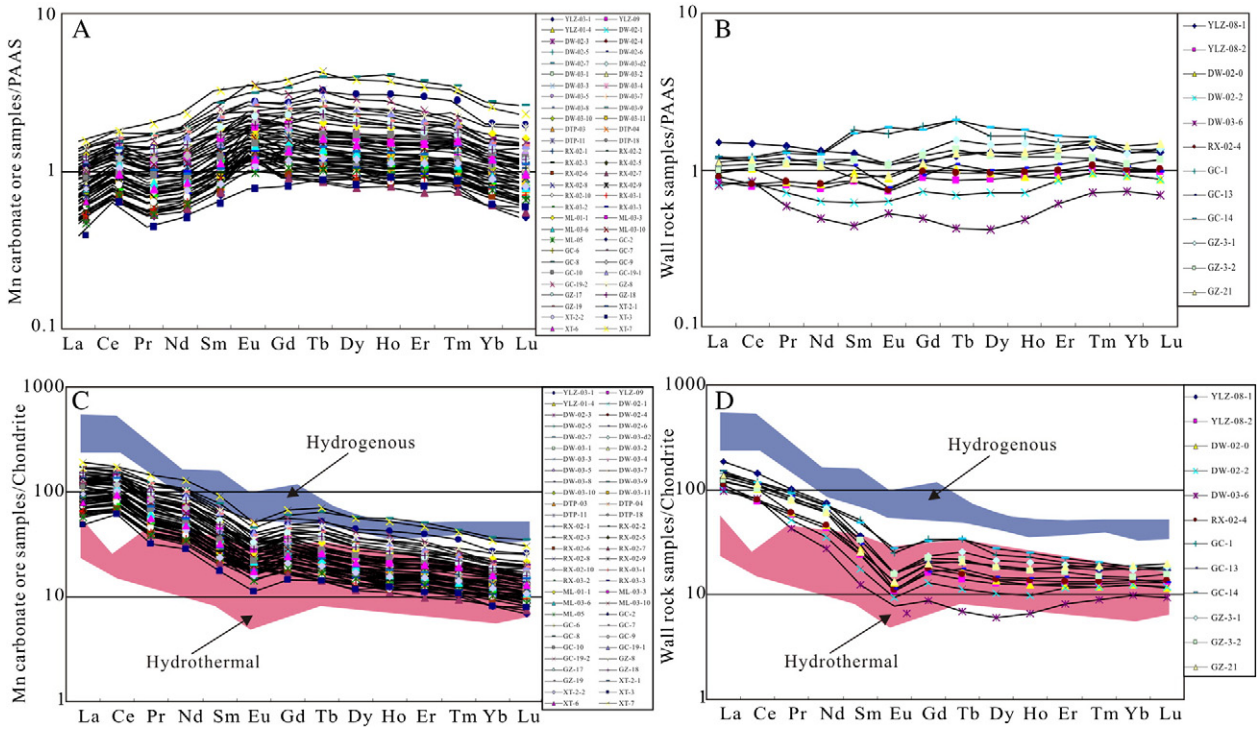

Fig. 11. PAAS-normalized and chondrite-normalized REE patterns of ores and wall rocks from the Nanhuan manganese deposits in the southeastern Yangtze Platform, China. The PAAS data are from (Taylor and McLennan, 1985), chondrite data are from Boynton (1984), and the REE patterns of hydrogenous and hydrothermal deposits are from Oksuz (2011); the "sample no." is the same as that in Table 2.

activities probably provided some amount of manganese, but this could not be the main manganese source for the deposits. So were terrigenous weathering and submarine hydrothermal processes the main manganese sources? This will be discussed in more detail below.

The $\delta^{34}S$ values of pyrite from manganese-bearing rock series are very high. Sulfur from sulfide in marine sediments mainly originates from the reduction of sulfate in seawater. Thus, the sulfur isotopic composition of sulfide depends on isotope fractionation processes during sulfate reduction (Strauss, 1999). In the inorganic reactions, ^{32}S–O bonds are broken easier than ^{34}S–O bonds, which leads to a ^{32}S enrichment of H_2S reduced from sulfate amounting to ~22‰ compared to sulfate (Harrison and Thode, 1958). However, if the SO_4^{2-} concentration is very low, sulfur isotope fractionation between sulfide and sulfate will decrease with the decreasing concentrations of sulfate. When the SO_4^{2-} concentration is extremely low, sulfur isotope fractionation is close to zero (Harrison and Thode, 1958; Strauss, 1993). Therefore, to form pyrite with very high $\delta^{34}S$, the $\delta^{34}S$ of sulfate should have been high and the sulfate concentration in seawater should have been extremely low.

In the seawater, the sulfate concentration was extremely low and this resulted in very low H_2S concentrations reduced from sulfate. The content of Fe was low in the samples (1.51–7.18%, average 2.76%), and a strong negative correlation between the $\delta^{34}S$ values of pyrite and average Fe contents was detected ($R = -0.83$) (Fig. 15). With lower concentrations of sulfate in the seawater, there would have been smaller levels of sulfur isotopic fractionation between SO_4^{2-} and H_2S and higher $\delta^{34}S$ values for pyrites. There also would have been lower H_2S concentrations reduced from sulfate, which may have led to the lower Fe concentrations, as pyrite was the main occurrence type of Fe in the ores.

As can be seen from Fig. 16, pyrites with very high $\delta^{34}S$ values exist in the Tiesiao Formation. The $\delta^{34}S$ values of pyrites reach peak levels in the manganese-bearing rock series and decline rapidly above them. This can be attributed to the very low concentration and extreme $\delta^{34}S$ enrichment of sulfate in the restricted basins (Wu et al., 2014; Wu et al., 2015). During the glacial period, the rate of sulfate reduction exceeded that of sulfate replenishment, so that residual sulfate in the restricted basins had low concentrations and considerably high $\delta^{34}S$ values. After the glacial period, bioproductivity at the ocean surface increased and the sulfate-minimum zone formed at the bottom of the ocean as organic matter sank (Li et al., 1999; Logan et al., 1995). The sulfate-minimum zone cut off sulfate replenishment and provided nutrients for sulfate reducing bacteria. Therefore, the rates of sulfate reduction were accelerated and the sulfur isotope fractionation between sulfide and sulfate decreased further. Therefore, the manganese-bearing rock series, which contain a large amount organic matter, displayed the peak $\delta^{34}S$ values for pyrites (Fig. 16). The sealing properties of the basins made the $\delta^{34}S$ values of pyrites from the same deposit fluctuate within a narrow range. Additionally, the $\delta^{34}S$ values of pyrites from different deposits that fluctuated over a wide range can be attributed to the differences in sealing properties of the basins. Specifically, the pyrites in better sealed basins have higher $\delta^{34}S$ values than the pyrites in other basins. As the rift continued to be extended, the restricted basins began to open and the sulfate that was depleted in $\delta^{34}S$ was introduced into the basins; consequently, the $\delta^{34}S$ values decrease from the bottom up along the profiles. Above the manganese-bearing rock series, the $\delta^{34}S$ values of pyrites decline rapidly because the restricted sedimentary environment had changed to the normal marine environment.

The pyrites in the manganese-bearing rock series mainly occur as disseminated, banded, nodular structures and the textures are framboidal and euhedral–subhedral. They were formed in the process of syngenetic sedimentation/diagenesis under an environment similar to the one where rhodochrosite and manganocalcite formed. Zhang (2014) analyzed the sulfur isotopic compositions of framboidal pyrites from the Xixibao and Gucheng deposits by using nano secondary ion mass spectrometry (NanoSIMS) and found that the framboidal pyrites also had very high $\delta^{34}S$ values with an average

Table 5
Organic carbon contents and isotopic compositions for organic carbon, inorganic carbon, and oxygen in samples from the Nanhuan manganese deposits in the southeastern Yangtze Platform, China.

Deposit	Sample	Rock (ore) type	Organic carbon %	Organic carbon isotope $\delta^{13}C_{V\text{-}PDB}$ ‰	Carbonate carbon isotope $\delta^{13}C_{V\text{-}PDB}$ ‰	Carbonate oxygen isotope $\delta^{18}O_{V\text{-}PDB}$ ‰	$\delta^{18}O_{SMOW}$ ‰
Datangpo	DTP-05	Mn carbonate ore	–	–	−7.52	−6.59	24.1
	DTP-22	Mn carbonate ore	–	–	−10.84	−7.69	22.9
Dawu	DW-03-d2	Mn carbonate ore	2.29	−33.38	−8.27	−12.34	18.1
	DW-03-1	Mn carbonate ore	1.62	−33.15	−8.94	−7.70	22.9
	DW-03-2	Mn carbonate ore	1.53	−32.90	−9.04	−7.88	22.7
	DW-03-3	Mn carbonate ore	1.37	−32.07	−7.59	−7.25	23.4
	DW-03-4	Mn carbonate ore	2.02	−33.46	−9.04	−8.16	22.4
	DW-03-5	Mn carbonate ore	1.97	−33.09	−8.29	−10.05	20.5
	DW-03-6	Mn-bearing shale	2.45	−33.24	−6.84	−11.49	19.0
	DW-03-7	Mn carbonate ore	2.77	−33.87	−9.70	−9.33	21.2
	DW-03-8	Mn carbonate ore	2.05	−33.62	−9.07	−9.69	20.9
	DW-03-9	Mn carbonate ore	2.82	−33.83	−9.32	−10.61	19.9
	DW-03-10	Mn carbonate ore	3.43	−33.74	−8.54	−10.50	20.0
	DW-03-11	Mn carbonate ore	2.43	−33.61	−8.54	−11.84	18.7
	DW-12-6	Mn carbonate ore	–	–	−9.15	−7.25	23.4
	DW-13-2	Mn carbonate ore	–	–	−9.22	−7.65	23.0
	DW-13-3	Mn carbonate ore	–	–	−7.34	−6.45	24.2
	DW-13-5	Mn-bearing shale	–	–	−7.39	−8.51	22.1
	DW-13-6	Mn-bearing shale	–	–	−6.85	−12.71	17.8
	DW-02-0	Mn-bearing shale	–	–	−7.32	−9.48	21.1
	DW-02-1	Mn carbonate ore	–	–	−9.04	−7.51	23.1
	DW-02-3	Mn carbonate ore	–	–	−9.45	−7.91	22.7
	DW-02-4	Mn carbonate ore	–	–	−8.81	−7.44	23.2
	DW-02-5	Mn carbonate ore	–	–	−8.80	−8.61	22.0
	DW-02-6	Mn carbonate ore	–	–	−9.95	−7.76	22.9
Xiushan	RX-02-1	Mn carbonate ore	1.89	−33.40	−6.61	−6.27	24.4
	RX-02-2	Mn carbonate ore	1.86	−33.55	−6.52	−6.84	23.8
	RX-02-3	Mn carbonate ore	2.32	−33.55	−6.33	−6.74	23.9
	RX-02-5	Carbonaceous shale	2.33	−33.53	−8.41	−5.10	25.6
	RX-02-6	Mn carbonate ore	2.05	−33.60	−8.63	−5.11	25.6
	RX-02-7	Mn carbonate ore	1.99	−33.97	−9.14	−6.56	24.1
	RX-02-8	Mn carbonate ore	2.28	−33.55	−7.64	−6.27	24.4
	RX-02-9	Mn carbonate ore	2.44	−33.47	−8.56	−5.65	25.0
	RX-02-10	Mn carbonate ore	2.44	−33.77	−7.82	−3.59	27.2
	RX-04	Mn carbonate ore	–	–	−8.47	−5.40	25.3
	RX-07	Mn-bearing shale	–	–	−7.63	−8.76	21.8
Minle	ML-03-3	Mn carbonate ore	–	–	−8.33	−7.19	23.4
	ML-05	Mn carbonate ore	–	–	−9.11	−4.67	26.0
Gucheng	GC-02	Mn carbonate ore	–	–	−3.12	−9.42	21.2
	GC-06	Mn carbonate ore	–	–	−4.02	−4.94	25.8
	GC-07	Mn carbonate ore	–	–	−2.67	−7.99	22.6
	GC-08	Mn carbonate ore	–	–	−2.53	−8.12	22.5
	GC-09	Mn carbonate ore	–	–	−2.41	−8.77	21.8
	GC-10	Mn carbonate ore	–	–	−2.41	−8.85	21.7
	GC-19-1	Mn carbonate ore	–	–	−3.53	−4.71	26.0
	GC-19-2	Mn carbonate ore	–	–	−3.84	−5.77	24.9
Xiangtan	XT-2-1	Mn carbonate ore	–	–	−8.51	−6.32	24.3
	XT-2-2	Mn carbonate ore	–	–	−9.38	−6.06	24.6
	XT-3	Mn carbonate ore	–	–	−8.40	−6.17	24.5
	XT-6	Mn carbonate ore	–	–	−6.96	−8.38	22.2

$\delta^{18}O_{SMOW} = 1.03086 \times \delta^{18}O_{V\text{-}PDB} + 30.86$.

of 44.48‰ (Xixibao) and 55.82‰ (Gucheng) Therefore, the $\delta^{34}S$ values of all the pyrites in the manganese-bearing rock series are very high and the restricted basins were important environments for the formation of manganese ores. The ores occur with micritic and microlitic textures and massive and laminated structures, which indicate that the ores formed in a low-energy environment. This is consistent with the environment of restricted basins.

The manganese from terrigenous weathering would have been limited as the ores formed in the restricted basins. Otherwise, the sulfate would have been introduced into the basins together with terrigenous manganese, which would have decreased the $\delta^{34}S$ values of pyrites. Therefore, we suggest that the deposits mainly originated from submarine hydrothermal processes and that terrigenous weathering was a secondary source. Interbedded tuffaceous siltstone occur in the Datangpo, Daotuo, and Guzhang deposits, which indicates that the submarine hydrothermal fluids were probably related to magmatism and/or volcanism.

The ores and wall rocks are enriched in organic carbon with an average of 2.21%. The organic carbon isotopic compositions ($\delta^{13}C_{V\text{-}PDB}$) range from −32.07‰ to −33.97‰ with an average of −33.44‰. The inorganic carbon isotopic compositions ($\delta^{13}C_{V\text{-}PDB}$) of carbonates in Gucheng range from −2.41‰ to −4.02% (average −3.07%), and in other deposits the values range from −6.33‰ to −10.84‰ (average −8.36‰).

The samples were enriched in organic carbon and the high organic carbon flux to the basins was from enhanced plankton productivity in the continental margin (Roy, 2006). The large amount of organic carbon, which was depleted in ^{13}C, buried in sediments would have caused carbon isotopic fractionation between organic carbon and inorganic carbon in seawater (Zhang et al., 2003a). Therefore, the inorganic carbon dissolved in seawater would have been enriched in ^{13}C. However, the inorganic carbon derived from buried organic carbon would have been depleted in ^{13}C, as it inherited the carbon isotopic compositions of organic carbon (Zhang et al., 2003a). The manganese carbonates all

Table 6
Sulfur isotopic compositions of pyrite from the Nanhuan manganese deposits in the southeastern Yangtze Platform, China.

Location	Sample	Rock (ore) type	$\delta^{34}S_{VCDT}$ (‰)
Yanglizhang	YLZ-16	Mn carbonate ore	52.2
Dawu	DW-02-1	Carbonaceous shale	48.2
	DW-02-2	Carbonaceous shale	47.5
	DW-02-3	Mn carbonate ore	48.2
	DW-03-d2	Carbonaceous shale from hanging wall	37.9
	DW-03-0	Mn carbonate ore	43.8
	DW-03-1	Mn carbonate ore	44.3
	DW-03-2	Mn carbonate ore	43.7
	DW-03-3	Mn carbonate ore	50.9
	DW-03-4	Mn carbonate ore	50.1
	DW-03-5	Mn carbonate ore	49.3
Dtangpo	DTP-07-2	Mn carbonate ore	61.3
	DTP-07-1	Mn carbonate ore	61.4
	DTP-09	Mn carbonate ore	62.6
	DTP-10	Mn carbonate ore	61.7
	DTP-19	Carbonaceous shale	61.6
	DTP-24	Carbonaceous shale	62.5
Xiushan	RX-02-2	Mn carbonate ore	50.5
	RX-03-5	Mn carbonate ore	49.8
Minle	ML-03-8	Mn carbonate ore	59.4
	ML-04	Mn carbonate ore	56.8
	GC-01	Carbonaceous shale	48.5
Gucheng	GC-02	Mn carbonate ore	61.6
	GC-03	Conglomerate from footwall	54.6
	GZ-1	Carbonaceous shale	53.7
	GZ-2	Carbonaceous shale	49.7
Guzhang	GZ-3	Carbonaceous shale	51.3
	GZ-4	Carbonaceous shale	53.2
	GZ-5	Mn carbonate ore	53.2

display depleted ^{13}C values, which indicates that the carbon not only originated from dissolved inorganic carbon in seawater, but also from organic carbon.

5.2. Formation of manganese carbonates

Previous studies have shown that the ocean of the Nanhuan Period was stratified in the study area with a surface layer consisting of an oxidizing environment and a deep water layer consisting of a reducing environment (Li et al., 2012). This stratified ocean suggested by the types of trace elements in the sediments. Researchers have proposed that ratios of Th/U, V/Cr, and V/(V + Ni) can be good indexes of redox conditions in sedimentary environments (Jones and Manning, 1994). The Th/U ratios vary from 0 to 2, which is indicative of an anoxic environment; in contrast, Th/U ratios that are >3.8 are indicative of oxic environments (Kimura and Watanabe, 2001). V/Cr values that are <2 represent oxic depositional conditions, 2.00 < V/Cr < 4.25 values represent suboxic conditions, and V/Cr values that are >4.25 represent anoxic conditions (Jones and Manning, 1994). High V/(V + Ni) (0.84–0.89) indicates the presence of H_2S in a strongly stratified water column (Hatch and Leventhal, 1992). Intermediate V/(V + Ni) (0.54–0.82) indicates a less strongly stratified anoxic water column, while low V/(V + Ni) (0.46–0.60) indicates a weakly stratified, dysoxic water column (Hatch and Leventhal, 1992).

The results from this study are as follows. The Th/U ratios vary from 1.67 to 4.86 with an average of 3.35 in ores, and they vary from 3.06 to 5.43 with an average of 4.04 in wall rocks. The V/Cr ratios vary from 1.29 to 5.97 with an average of 3.16 in ores, and they vary

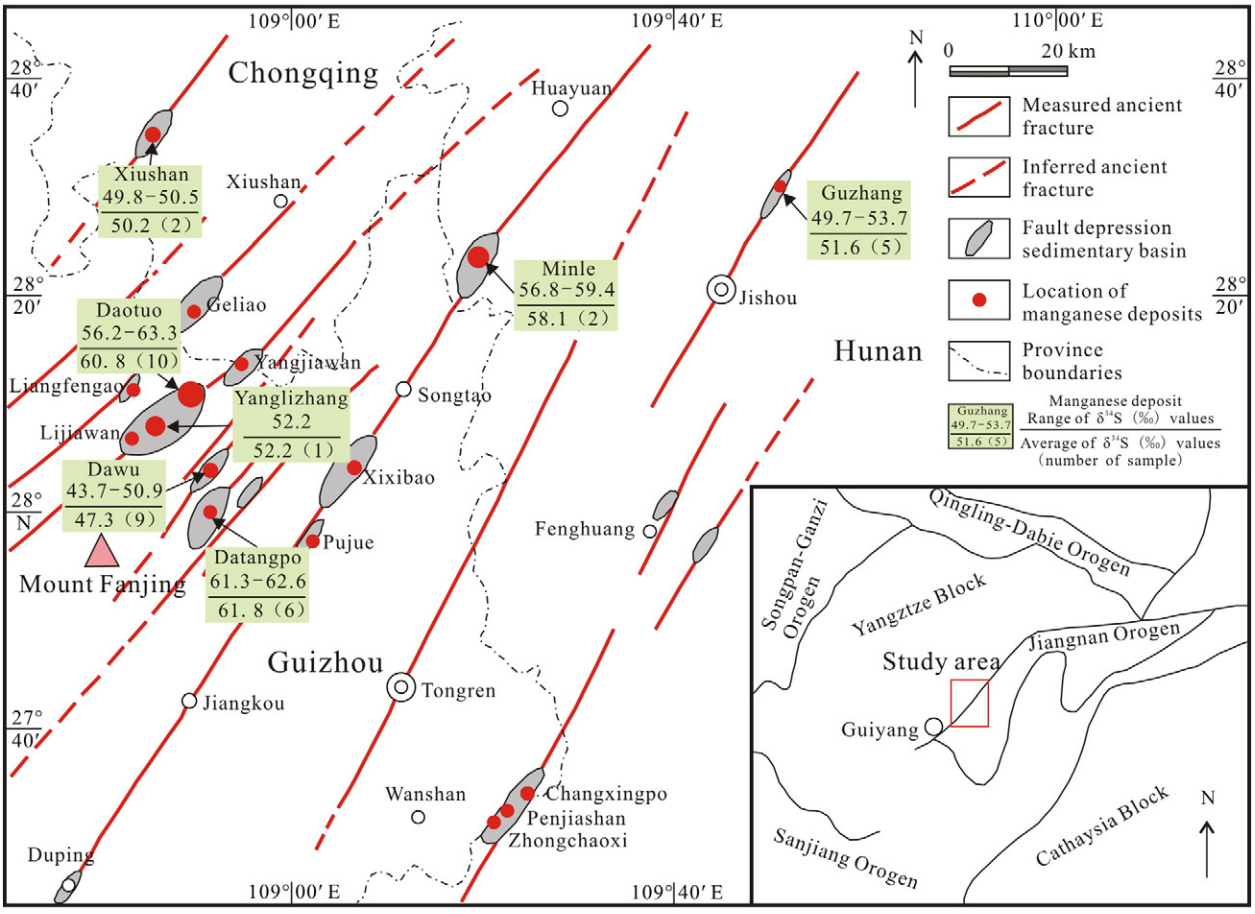

Fig. 12. Distribution of $\delta^{34}S$ values for pyrite from the Nanhuan manganese deposits in the southeastern Yangtze Platform, China (based on Zhou et al., 2013). The $\delta^{34}S$ values of pyrite are from Tables 6 and 7.

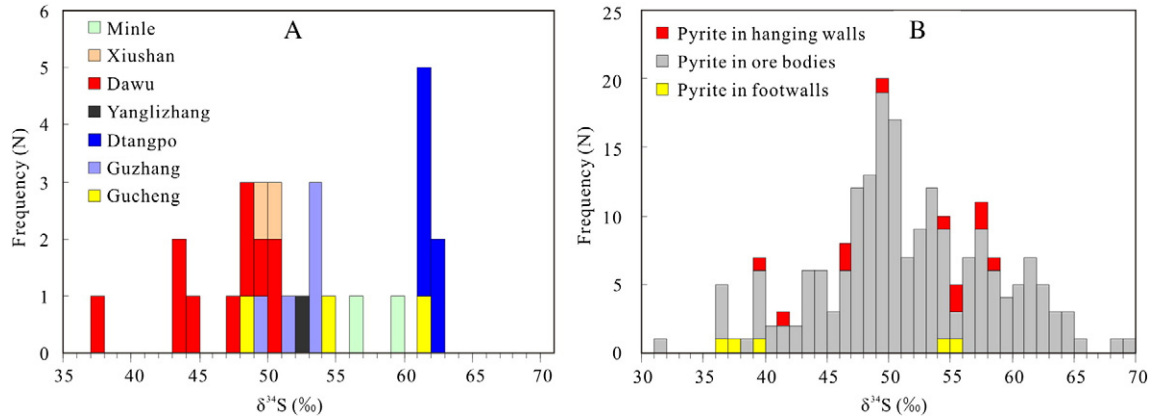

Fig. 13. Histogram of sulfur isotopic compositions for pyrite from the Nanhuan manganese deposits in the southeastern Yangtze Platform, China. (A) Data are from Table 6 of this study; (B) data are from this study and earlier studies (Chu et al., 2001; Feng et al., 2010; Li et al., 1996, 1999, 2012; Liu et al., 1989, 2006; Tang, 1990; Tang and Liu, 1999; Wang et al., 1985; Zhang et al., 2013b; Zhou, 2008; Zhu et al., 2013).

from 1.15 to 2.88 with an average of 2.22 in wall rocks. The V/(V + Ni) ratios vary from 0.54 to 0.86 with an average of 0.71 in ores, and they vary from 0.51 to 0.76 with an average of 0.64 in wall rocks. Overall, the trace element ratios indicate that the depositional environment was reductive and some local areas (maybe at the surface) were oxidic.

Some studies have shown that patterns of molybdenum–uranium covariation can be linked to variation in benthic redox conditions, the operation of particulate shuttle (a particulate medium that can adsorb trace-metal elements and enhances the export of aqueous trace-metal elements to the sediment) within the water column, and the evolution of water mass chemistry (Algeo and Tribovillard, 2009; Tribovillard et al., 2012). That is because U uptake commences at the Fe (II)–Fe(III) redox boundary earlier than Mo uptake, which requires the presence of H_2S; additionally, transfer of Mo to the sediment can be accelerated through a particulate Mn–Fe-oxyhydroxide shuttle, whereas U is unaffected by this process (Algeo and Tribovillard, 2009).

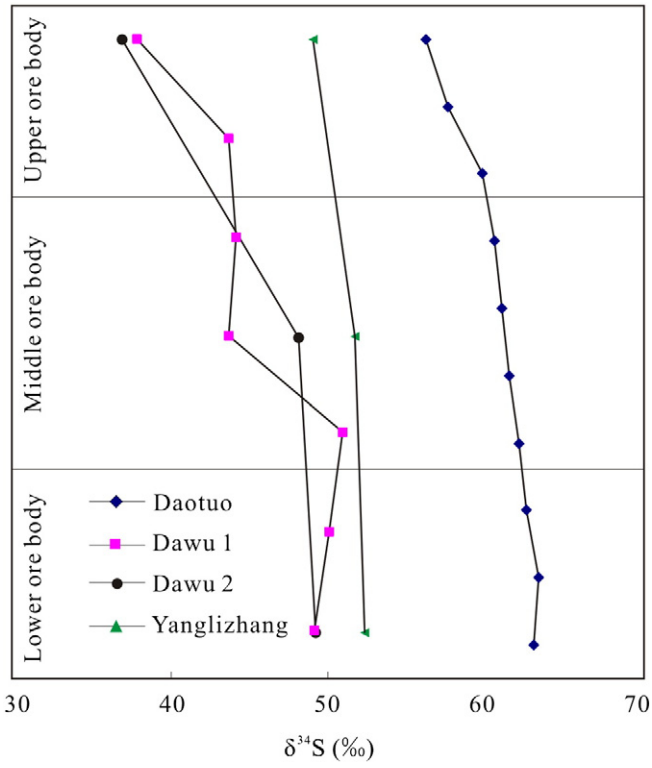

Fig. 14. Sulfur isotopic variations of pyrite along the profiles from the Nanhuan manganese deposits in the southeastern Yangtze Platform, China.
Data for the Daotuo manganese deposit are from Zhu et al. (2013), data for Dawu 1 are from this study (see Table 6), and data for Dawu 2 and Yanglizhang are from Liu et al. (1989).

The Mo/TOC values range from 0.22 to 4.72 (except for sample DW-03-6, which had a value of 19.81) with an average of 1.27, which are significantly lower than those in the Black Sea (Mo/TOC average of ~4.5), and this is indicative of an extremely restricted depositional environment (Fig. 17). It is similar to the environment indicated by the sulfur isotopic compositions of pyrites. In the Mo_{EF} versus U_{EF} diagram (Fig. 18), the samples mainly fall in the suboxic region to the particulate shuttle region, which suggests that Mn–Fe-oxyhydroxides were present in the sediments. That is because Mn–Fe-oxyhydroxide can serve as a particulate shuttle to accelerate the transfer of Mo to the sediments, which increases the Mo/U ratios in the samples.

The stratified ocean is favorable for the enrichment, precipitation, and transfer of manganese. In marine sediments, Mn carbonate precipitation is controlled by a very high concentration of dissolved Mn^{2+} in the pore water in association with adequate dissolved bicarbonate, whereby the levels exceed the solubility product of Mn carbonate (Calvert and Pedersen, 1993; Calvert and Pedersen, 1996; Kuleshov, 2011; Roy, 2006). Such an enhanced supply of dissolved Mn^{2+} is considered possible only in stratified basins where the Mn-oxyhydroxide (manganese occurred as Mn_3O_4 and γ-MnOOH) precipitate from overlying oxic seawater is buried into a reducing zone (Roy, 2006). Then, a very high level of dissolved Mn^{2+} can be attained. Manganese carbonates are formed by diagenetic reactions of the dissolved Mn^{2+} with organically derived bicarbonate in anoxic zones. Such diagenetic Mn carbonates are depleted in ^{13}C (Okita et al., 1988; Okita and Shanks, 1992).

The manganese, which mainly originated from submarine hydrothermal fluids, was enriched in the deep waters of the basins as dissolved Mn^{2+}. Then, the Mn^{2+} was oxidized to insoluble Mn-oxyhydroxide in the overlying oxic seawater and it precipitated into the sediments. In the diagenetic reactions, the buried Mn-oxyhydroxide was reduced to Mn^{2+} and bicarbonate was derived from the oxidation of organic carbon. In such a process, the Mn carbonates, which are hosted in black shales and depleted in ^{13}C, were formed.

The formation of Mn carbonates is also supported by the trace and REE elements. The chondrite-normalized REE patterns showed that the patterns of ores and wall rocks both lay between the hydrogenous and hydrothermal deposits (Fig. 11C, D). As the deposits were formed in the restricted basins, supplementation of REE elements

Table 7
Statistical results for sulfur isotope compositions of pyrite from the Nanhuan manganese deposits in the southeastern Yangtze Platform, China.

Deposit	$\delta^{34}S_{VCDT}$ (‰)	Number of samples	Average $\delta^{34}S_{VCDT}$ (‰)	Average content of Fe	Source
Datangpo	61.3–62.6	6	61.8	1.90	This work
	48.6–57.8	7	54.0	/	Li et al. (1996), Li et al. (1999), Wang et al. (1985), Zhou (2008)
Minle	56.8–59.4	2	58.1	2.53	This work
	38.6–69.0	76	52.7	/	Feng et al. (2010), Li et al. (1996), Li et al. (1999), Li et al. (2012), Tang (1990), Tang and Liu (1999), Wang et al. (1985)
Yanglizhang	52.2	1	52.2	2.90	This work
	39.2–52.9	26	48.8	/	Wang et al. (1985), Zhou (2008)
Dawu	43.7–50.9	9	47.3	3.07	This work
	36.9–49.3	14	44.5	/	Wang et al. (1985), Zhou (2008)
Daotuo	56.2–63.3	10	60.8	2.14	Zhu et al. (2013)

In the table, "/" indicates "not detected."

was limited. However, the Mn-oxyhydroxide can adsorb and accelerate precipitation of the REE elements. Hence, the total REE elements of the studied deposits are between those of hydrogenous and hydrothermal deposits. The Mn-oxyhydroxide also can oxidize Ce^{3+} to Ce^{4+} and adsorb Co and Mo, which led to the positive Ce, Co, Mo anomalies in the samples (Ce/Ce* average of 1.23 in ores). This is also shown by the presence of Mn-oxyhydroxide in the U_{EF}–Mo_{EF} diagram (Fig. 18). In addition, Zhang (2014) studied the iron isotopic compositions of pyrites from manganese deposits in the study area and showed that the pyrites in the manganese-bearing rock series are significantly enriched in heavy iron isotopes compared to the overlying and underlying strata. The average $\delta^{56}Fe_{-IRMM}$ value of pyrites from the top of the Tiesiao Formation and the first member of the Datangpo Formation is +0.51%. This is because a part of the Fe was oxidized in the overlying oxygenated water and precipitated as iron oxides, which were enriched in heavy iron isotopes. Then, the pyrites, which were formed from the reduction of iron oxides, inherited their iron isotopic compositions and were enriched in heavy iron isotopes (Zhang, 2014). This also suggests that the Fe and Mn were oxidized and precipitated as oxides and hydroxides, and then, they were reduced to manganese carbonates and pyrites in the diagenetic reactions.

6. Conclusions

Analyses of the metallogenic geological conditions of the Nanhuan manganese deposits revealed that the ore bodies occur in the black shale series from the basal Datangpo Formation and metallogenic processes and morphology of ore bodies both were controlled by the sedimentary environments of restricted basins. The extremely low concentrations of sulfate in the restricted basins resulted in the high $\delta^{34}S$ values of pyrite. The manganese mainly originated from submarine hydrothermal processes. Volcanism and terrigenous weathering probably provided minor amounts of manganese to the deposits. The manganese was enriched in the deep anoxic waters of the basins as dissolved Mn^{2+}. Then, the Mn^{2+} was oxidized to Mn-oxyhydroxide in the overlying oxic seawater and it precipitated into the sediments. In the diagenetic reactions, the buried Mn-oxyhydroxide

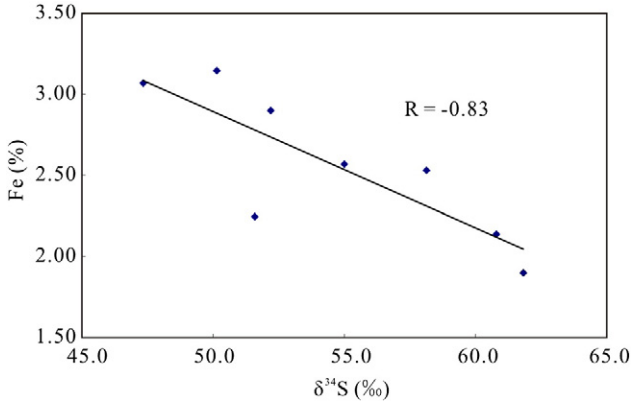

Fig. 15. Correlation diagram of pyrite $\delta^{34}S$ values and average Fe contents of samples from the Nanhuan manganese deposits in the southeastern Yangtze Platform, China.

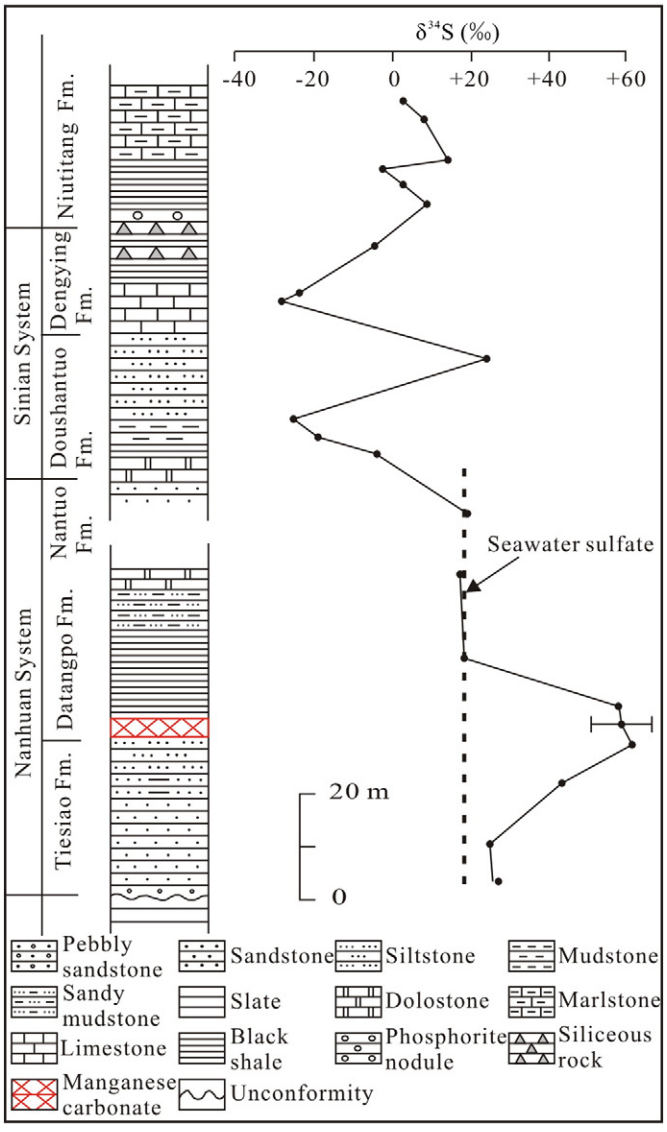

Fig. 16. Evolution of sulfur isotopic compositions in pyrite from the Nanhuan and Sinian strata in the southeastern Yangtze Platform, China (Li et al., 1999).

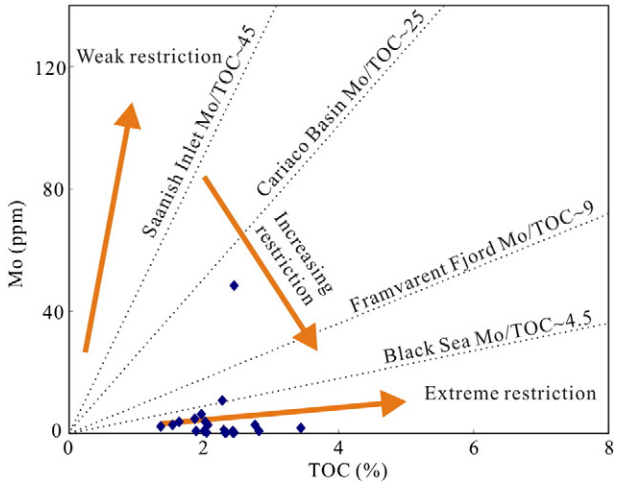

Fig. 17. Diagram of the total organic carbon content versus Mo concentration ([TOC] versus [Mo]) for samples from the Dawu and Rongxi deposits (based on Tribovillard et al., 2012). Data are from Tables 4 and 5.

was reduced to Mn^{2+} and bicarbonate was derived from the oxidation of organic carbon in the pore water. In such a process, the Mn carbonates, which were depleted in ^{13}C, were formed. Therefore, the Nanhuan manganese deposits in the southeastern Yangtze Platform, which are hosted in the black shale series, are hydrothermal–sedimentary/diagenetic type deposits.

Conflict of interest

This manuscript has not been published or presented elsewhere in part or in entirety, and it is not under consideration by another journal. All the authors have approved the manuscript and agree with submission to your esteemed journal. There are no conflicts of interest to declare.

Acknowledgments

The authors are grateful to Prof. Franco Pirajno, Prof. Duofu Chen and Dr. Lingang Xu for their helpful suggestions toward improving the quality of this manuscript. This research was financially supported by the 12th Five-Year Plan project of the State Key Laboratory of Ore-deposit Geochemistry, Chinese Academy of Sciences (SKLODG-ZY125-08) and the Natural Science Foundation of China (NSFC No. 41573039).

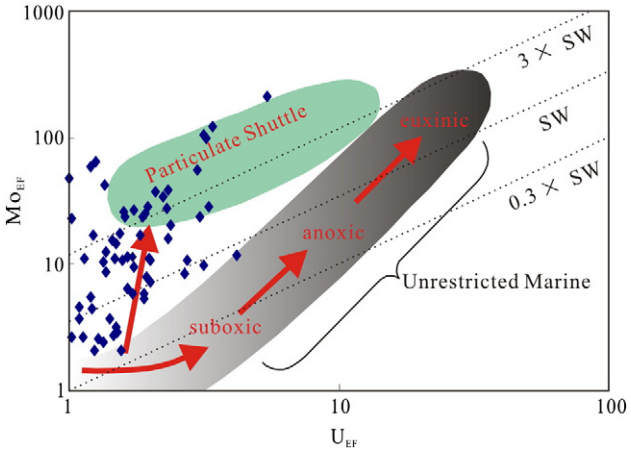

Fig. 18. Mo_{EF} versus U_{EF} diagram for samples from the Nanhuan manganese deposits in the southeastern Yangtze Platform, China. $X_{EF} = [(X/Al)_{sample} / (X/Al)_{PAAS}]$, and X and Al stand for the weight concentrations of element X and Al, respectively. Samples were normalized using the Post-Archean average Australian shale (PAAS) compositions of Taylor and McLennan (1985). Dotted lines show Mo/U molar ratios equal to the seawater value (1 × SW) and to fractions thereof (0.3 × SW, 0.1 × SW) (based on Algeo and Tribovillard, 2009; Tribovillard et al., 2012). Data are from Table 4.

Appendix A. Supplementary data

Supplementary data associated with this article can be found in the online version, at doi:http://dx.doi.org/10.1016/j.oregeorev.2015.12.003. These data include the Google map of the most important areas described in this article.

References

Algeo, T., Tribovillard, N., 2009. Environmental analysis of paleoceanographic systems based on molybdenum–uranium covariation. Chem. Geol. 268 (3), 211–225.
Boynton, W.V., 1984. Cosmochemistry of the rare earth elements, meteorite studies. In: Henderson, P. (Ed.), Rare Earth Element Geochemistry. Elsevier, pp. 63–144.
Calvert, S., Pedersen, T., 1993. Geochemistry of recent oxic and anoxic marine sediments, implications for the geological record. Mar. Geol. 113 (1), 67–88.
Calvert, S., Pedersen, T., 1996. Sedimentary geochemistry of manganese; implications for the environment of formation of manganiferous black shales. Econ. Geol. 91 (1), 36–47.
Cao, H.Q., 2011. The Evaluation of Prospecting Rights of Yuquan Manganese Ore in Xiushan County, Chongqing. Chengdu University of Technology, Chengdu, pp. 1–37 (in Chinese with English abstract).
Chen, D.F., Chen, X.P., 1992. Geological and geochemical characteristics of Songtao hydrothermal sedimentary manganese deposit, Guizhou. Acta Sedimentol. Sin. 10 (4), 35–43 (in Chinese with English abstract).
Chu, X.L., Li, R.W., Zhang, T.G., Zhang, Q.R., 2001. Implication of ultra-high $\delta^{34}S$ values of pyrite in manganese mineralization meds of Datangpo stage. Bull. Mineral. Petrol. Geochem. 20 (4), 320–322 (in Chinese with English abstract).
Condon, D., Zhu, M., Bowring, S., Wang, W., Yang, A., Jin, Y., 2005. U–Pb ages from the neoproterozoic Doushantuo Formation, China. Science 308 (5718), 95–98.
Du, G.Y., Zhou, Q., Yuan, L.J., Xie, X.F., 2013. Spatial distribution characters and prospecting direction analyses on rebody of Yanglizhang manganese deposit in Songtao of east Guizhou. Guizhou Geol. 30 (3), 177–184 (in Chinese with English abstract).
Fan, D., Yang, P., 1999. Introduction to and classification of manganese deposits of China. Ore Geol. Rev. 15, 1–13.
Feng, L.-J., Chu, X.-L., Huang, J., Zhang, Q.-R., Chang, H.-J., 2010. Reconstruction of paleoredox conditions and early sulfur cycling during deposition of the Cryogenian Datangpo Formation in South China. Gondwana Res. 18 (4), 632–637.
Fu, S.Y., 2005. Geological character of Huayuan–Guzhang manganese ore deposit, indicator and direction. China's Manganese Industry. 23(1), pp. 23–25 (in Chinese with English abstract).
Guizhou Geological survey, 2009. Potential survey report of manganese ore deposits in Songtao–Tongren China. pp. 1–79 (in Chinese).
Harrison, A., Thode, H., 1958. Mechanism of the bacterial reduction of sulphate from isotope fractionation studies. Trans. Faraday Soc. 54, 84–92.
Hatch, J., Leventhal, J., 1992. Relationship between inferred redox potential of the depositional environment and geochemistry of the Upper Pennsylvanian (Missourian) Stark shale member of the Dennis limestone, Wabaunsee County, Kansas, USA. Chem. Geol. 99 (1), 65–82.
He, Z.W., Yang, R.D., Gao, J.B., Cheng, W., Liu, S., Zhang, W.F., 2014. The geochemical characteristics and sedimentary environment of manganese-bearing rock series of Daotuo manganese deposit, Songtao County of Guizhou Province. Geol. Rev. 60 (05), 1061–1075 (in Chinese with English abstract).
Hou, B.D., Yuan, L.J., Zhan, P.C., 2011. Geological characteristics and analysis on prospecting potential of Yanglizhang manganese ore deposit in Songtao of Guizhou. Mineral Resour. Geol. 25 (1), 47–52 (in Chinese with English abstract).
Hu, X.Y., 2009. Determine the major element concentrations of carbonate rocks using X-ray fluorescence spectrometry. Acta Mineral. Sin. 598 (S), 597 (in Chinese).
Jiang, G., Sohl, L.E., Christie-Blick, N., 2003. Neoproterozoic stratigraphic comparison of the Lesser Himalaya (India) and Yangtze block (south China), paleogeographic implications. Geology 31 (10), 917–920.
Jones, B., Manning, D.A., 1994. Comparison of geochemical indices used for the interpretation of palaeoredox conditions in ancient mudstones. Chem. Geol. 111, 111–129.
Kimura, H., Watanabe, Y., 2001. Oceanic anoxia at the Precambrian–Cambrian boundary. Geology 29 (11), 995–998.
Kuang, W.L., Li, X.Y., Yang, S.X., 2014. The mineralization geological characteristics and genesis of Minle type manganese deposit in northwestern of Hunan Province. Chin. J. Geol. 49 (1), 305–323 (in Chinese with English abstract).
Kuleshov, V., 2011. Manganese deposits, communication 1. Genetic models of manganese ore formation. Lithol. Miner. Resour. 46 (5), 473–493.
Li, R.W., Zhang, S.K., Lei, J.J., Shen, Y.A., Chen, J.S., Chu, X.L., 1996. Temporal and spacial varation in $\delta^{34}S$ values of pyrite from Sinian strata discussion on relationship between Yangtze Block and the late Proterozoic supercontinental. Chin. J. Geol. 31 (03), 209–217 (in Chinese with English abstract).
Li, R.W., Chen, J., Zhang, S., Lei, J., Shen, Y., Chen, X., 1999. Spatial and temporal variations in carbon and sulfur isotopic compositions of Sinian sedimentary rocks in the Yangtze platform, South China. Precambrian Res. 97 (1), 59–75.
Li, Z.X., Li, X., Kinny, P., Wang, J., Zhang, S., Zhou, H., 2003. Geochronology of Neoproterozoic syn-rift magmatism in the Yangtze Craton, South China and

correlations with other continents, evidence for a mantle superplume that broke up Rodinia. Precambrian Res. 122 (1), 85–109.
Li, C., Love, G.D., Lyons, T.W., Scott, C.T., Feng, L., Huang, J., Chang, H., Zhang, Q., Chu, X., 2012. Evidence for a redox stratified Cryogenian marine basin, Datangpo Formation, South China. Earth Planet. Sci. Lett. 331, 246–256.
Liu, X.F., Wang, Q.S., Gao, X.J., 1989. Mangenese Deposits of Guihzou, China. Guizhou People Press, Guiyang, pp. 1–194 (in Chinese).
Liu, T.b., Maynard, J.B., Alten, J., 2006. Superheavy S isotopes from glacier-associated sediments of the Neoproterozoic of south China, Oceanic anoxia or sulfate limitation? In: Kesler, S.E., Ohmoto, H. (Eds.), Evolution of Early Earth's Atmosphere, Hydrosphere, and Biosphere—Constraints From Ore Deposits. Geological Society of America Memoirs 198, pp. 205–222
Logan, G.A., Hayes, J., Hieshima, G.B., Summons, R.E., 1995. Terminal Proterozoic reorganization of biogeochemical cycles. Nature 376 (6535), 53–56.
Macdonald, F.A., Schmitz, M.D., Crowley, J.L., Roots, C.F., Jones, D.S., Maloof, A.C., Strauss, J.V., Cohen, P.A., Johnston, D.T., Schrag, D.P., 2010. Calibrating the cryogenian. Science 327 (5970), 1241–1243.
Ministry of Land and Resources of the People's Republic of China, 2014f. China Mineral Resources. Geological Publishing House, Beijing, pp. 1–36 (in Chinese).
Okita, P.M., Shanks, W.C., 1992. Origin of stratiform sediment-hosted manganese carbonate ore deposits, examples from Molango, Mexico, and TaoJiang, China. Chem. Geol. 99 (1), 139–163.
Okita, P.M., Maynard, J.B., Spiker, E.C., Force, E.R., 1988. Isotopic evidence for organic matter oxidation by manganese reduction in the formation of stratiform manganese carbonate ore. Geochim. Cosmochim. Acta 52 (11), 2679–2685.
Oksuz, N., 2011. Geochemical characteristics of the Eymir (Sorgun–Yozgat) manganese deposit, Turkey. J. Rare Earths 29 (3), 287–296.
Ouayang, L.M., Dai, T.G., Gong, J.H., 2011. Geological characters and genesis of Lannitian manganese deposit in Guzhang county, western Hunan,China. 178. Southern Metals, pp. 16–19 (in Chinese with English abstract).
Qi, L., Hu, J.D., Conrad, G., 2000. Determination of trace elements in granites by inductively coupled plasma mass spectrometry. Talanta 51 (3), 507–513.
Qin, Y., An, Z.Z., Wang, J.W., Li, D.P., 2013. The discovery and geological characteristics of the super-large sized Daotuo manganese deposit in Songtao, Guizhou. 4(04). Mineral Exploration, pp. 345–355 (in Chinese with English abstract).
Regional Geology Department of Geology and Mineral Resources, Ministry of Geology and Mineral Resources, 1983e. Geological Corpus of Chinese Manganese Deposits. Geological Publishing House, Beijing, pp. 1–386 (in Chinese).
Roy, S., 2006. Sedimentary manganese metallogenesis in response to the evolution of the Earth system. Earth Sci. Rev. 77, 273–305.
Strauss, H., 1993. The sulfur isotopic record of Precambrian sulfates, new data and a critical evaluation of the existing record. Precambrian Res. 63 (3), 225–246.
Strauss, H., 1999. Geological evolution from isotope proxy signals—sulfur. Chem. Geol. 161 (1), 89–101.
Tan, M.T., Lu, Z.X., Zhang, Y., 2009. Preliminary analysis on genesis of manganese deposit in Datangpo Formation, western Hubei Province. Resour Environ. Eng. 23 (2), 108–113 (in Chinese with English abstract).
Tang, S.Y., 1990. Isotopic geological study of manganese deposit in Minle area, Hunan Province. Acta Sedimentol. Sin. 8 (4), 77–84 (in Chinese with English abstract).
Tang, S., Liu, T., 1999. Origin of the early Sinian Minle manganese deposit, Hunan Province, China. Ore Geol. Rev. 15 (1), 71–78.
Taylor, S.R., McLennan, S.M., 1985. The Continental Crust, Its Composition and Evolution. Blackwell, Oxford, pp. 1–312.
Tribovillard, N., Algeo, T., Baudin, F., Riboulleau, A., 2012. Analysis of marine environmental conditions based onmolybdenum–uranium covariation—applications to Mesozoic paleoceanography. Chem. Geol. 324–325, 46–58.
Wang, Y.G., 1990. Old hot brine manganese deposit in a shallow-sea rift basin, an example from the Sinian manganese deposits in the Wuling Mountain area. Sediment. Geol. Tethyan Geol. 1, 39–45 (in Chinese with English abstract).
Wang, J., Li, Z.X., 2003. History of Neoproterozoic rift basins in South China, implications for Rodinia break-up. Precambrian Res. 122 (1), 141–158.
Wang, Y.G., Wang, L.X., Zhu, S.C., Xie, Z.Q., Chen, D.C., Zheng, S.F., Chen, Y.L., Zhu, H., 1985. The Stratigrcaphy, Sedimentary Environment and Manganese-forming Process of Datangpo Formation in Eastern Guizhou. Guizhou People Press, Guiayng, pp. 1–92 (in Chinese).
Wang, X.C., Li, X.H., Li, W.X., Li, Z.X., 2009. Variable involvements of mantle plumes in the genesis of mid-Neoproterozoic basaltic rocks in South China, a review. Gondwana Res. 15 (3), 381–395.
Wu, C., Zhang, Z., Zheng, C., Yao, J., 2014. Implication of ultra-high $\delta^{34}S$ values in pyrite from manganese deposits of the Datangpo Stage, Yangtze Platform, China. Acta Geol. Sin. 88 (Suppl. 2), 266–267.
Wu, C.Q., Cheng, Y., Zhang, Z.W., Xiao, J.F., Fu, Y.Z., Shao, S.X., Zheng, C.F., Yao, J.H., 2015. Geological implications of ultra-high $\delta^{34}S$ values of pyrite in manganese deposits of Nanhua Period in eastern Guizhou and adjacent areas, China. Geochimica 44 (3), 213–224 (in Chinese with English abstract).
Xie, Q.L., Chen, D.F., Chen, X.P., 1999. Characteristics of sedimentary organic matter in Songtao manganese deposits,Guizhou. Acta Sedimentol. Sin. 17 (2), 280–284 (in Chinese with English abstract).
Xie, X.F., Qin, Y., Wen, G.G., Xie, X.Y., 2014. Relation between Datangpo Formation and manganese mineralization in Songtao manganese mining area of Tongren in Guizhou. Guizhou Geol. 1 (31), 32–37 (in Chinese with English abstract).
Yang, S.X., Lao, K.T., 2006. Mineralization model for the manganese deposits in northwestern Hunan, an example from Minle manganese deposit in Huayuan, Hunan. Sediment. Geol. Tethyan Geol. 26 (2), 72–80 (in Chinese with English abstract).
Yang, R.D., Ouyang, Z.Y., Zhu, L.J., Wang, S.J., Jiang, L.J., Zhang, W.h., Gao, H., 2002. A new understanding of manganese carbonate deposit in early Sinian Datangpo stage. Acta Mineral. Sin. 22 (4), 329–334 (in Chinese with English abstract).
Yao, J.Q., Wang, L.M., Sun, C.G., Zhang, Q.C., 1995. The Study of Manganese Deposits From Southern Margin of Yangtze Platform and Adjacent Region. Metallurgical Industry Press, Beijing, pp. 1–236 (in Chinese with English abstract).
Yu, P.R., 2008. Geologic characters & prospect in Huayua Mingle Mn-ore deposit of Hunan. China's Manganese Industry. 26(4), pp. 9–13 (in Chinese with English abstract).
Zhang, F.F., 2014. The Formation Mechanism of Datangpo Manganese Ore Deposits During Nanhua Period in South China and the Paleo-redox Conditions of Nanhua Marine Basin. Chinese Academy of Geological Sciences, Beijing pp. 1–121 (in Chinese with English abstract).
Zhang, Q., Chu, X., Bahlburg, H., Feng, L., Dobrzinski, N., Zhang, T., 2003a. Stratigraphic architecture of the Neoproterozoic glacial rocks in the "Xiang-Qian-Gui" region of the central Yangtze Block, South China. Prog. Nat. Sci. 13 (10), 783–787.
Zhang, T.G., Chu, X.L., Feng, L.J., Zhang, Q.R., Guo, J.P., 2003b. The effects of the Neoproterozoic Snowball Earth on carbon and sulfur isotopic compositions in seawater. Acta Geosci. Sin. 24 (6), 487–493 (in Chinese with English abstract).
Zhang, S., Jiang, G., Zhang, J., Song, B., Kennedy, M.J., Christie-Blick, N., 2005. U–Pb sensitive high-resolution ion microprobe ages from the Doushantuo Formation in south China, constraints on late Neoproterozoic glaciations. Geology 33 (6), 473–476.
Zhang, S., Jiang, G., Han, Y., 2008. The age of the Nantuo Formation and Nantuo glaciation in South China. Terra Nova 20 (4), 289–294.
Zhang, F.F., Yan, B., Guo, Y.L., Zhu, X.K., Zhou, Q., Yang, D.Z., 2013a. Precipitation form of manganese ore deposit in Gucheng, Hubei Province, and its paleoenvironment implation. Acta Geol. Sin. 87 (02), 245–258 (in Chinese with English abstract).
Zhang, F.F., Zhu, X.K., Gao, Z.F., Cheng, L., Peng, Q.Y., Yang, D.Z., 2013b. Implication of the precipitation mode of manganese and ultra-high $\delta^{34}S$ values of pyrite in Mn-carbonate of Xixibao Mn ore deposit in northeastern Guizhou Province. Geol. Rev. 59 (02), 274–286 (in Chinese with English abstract).
Zhou, Q., 2008. Geological and Geochemical Characteristics of Cold Seep Carbonates of Neoproterozoic Nanhua Period and Their Significance for Manganese Ore Deposit in East Guizhou. China University of Geosciences, Wuhan, pp. 1–104 (in Chinese with English abstract).
Zhou, C., Robert, T., Xiao, S., Peng, Z., Yuan, X., Chen, Z., 2004. New constraints on the ages of Neoproterozoic glaciations in south China. Geology 32, 437–440.
Zhou, J.C., Wang, X.L., Qiu, J.S., 2009. Some Neoproterozoic geological events involved in the development of the Jiangnan Orogen. Geol. J. China Univ. 15 (4), 453–459 (in Chinese with English abstract).
Zhou, Q., Du, Y.S., Qin, Y., 2013. Ancient natural gas seepage sedimentary-type manganese metallogenic system and ore-forming model, a case study of "Datangpo type" manganese deposits formed in rift basin of Nanhua Period along Guizhou–Hunan–Chongqing border area. Mineral Deposits 32 (3), 457–466 (in Chinese with English abstract).
Zhou, W.D., Zhang, Z.W., Yuan, S.C., Wu, C.Q., Li, Y.J., 2014. Characteristics and mineralization epochs of the Bairong porphyry copper–molybdenum deposit in the Nyemo County, Tibet. Bull. Mineral. Petrol. Geochem. 33, 77–184 (in Chinese with English abstract).
Zhu, X.K., Peng, Q.Y., Zhang, R.B., An, Z.Z., Zhang, F.F., Yan, B., Li, J., Gao, Z.F., Tan, Y., Pan, W., 2013. Geological and geochemical characteristics of the Daotuo super-large manganese ore deposit at Songtao County in Guizhou Province. Acta Geol. Sin. 87 (09), 1335–1348 (in Chinese with English abstract).